Accepted Manuscript

A Non-local Plasticity Model of Stimulated Volume Evolution During Hydraulic Fracturing

Erfan Sarvaramini, Maurice B. Dusseault, Mohammad Komijani, Robert Gracie

PII: S0020-7683(18)30387-1
DOI: https://doi.org/10.1016/j.ijsolstr.2018.09.023
Reference: SAS 10127

To appear in: *International Journal of Solids and Structures*

Received date: 8 December 2017
Revised date: 17 September 2018
Accepted date: 19 September 2018

Please cite this article as: Erfan Sarvaramini, Maurice B. Dusseault, Mohammad Komijani, Robert Gracie, A Non-local Plasticity Model of Stimulated Volume Evolution During Hydraulic Fracturing, *International Journal of Solids and Structures* (2018), doi: https://doi.org/10.1016/j.ijsolstr.2018.09.023

A Non-local Plasticity Model of Stimulated Volume Evolution During Hydraulic Fracturing

Erfan Sarvaramini[a], Maurice B. Dusseault[b], Mohammad Komijani[a], Robert Gracie[a,*]

[a] *Department of Civil and Environmental Engineering, University of Waterloo, 200 University Ave W, Waterloo, ON Canada N2L 3G1*

[b] *Earth and Environmental Sciences Department, University of Waterloo, 200 University Ave W, Waterloo, ON Canada N2L 3G1*

Abstract

Hydraulic fracturing in naturally fractured rocks often leads to the creation of a stimulated zone in which the target rock formation is deformed and fractured by the reactivation and shear dilation of natural fractures and the plastic deformation, damaging, and fracturing of the bulk. In this paper, we present a novel mathematical model with the goal of simulating the evolution of the stimulated volume during hydraulic fracturing. This was achieved by introducing an equivalent continuum non-local poro-elastic-plastic zone of enhanced permeability for the stimulated region, characterized by an internal length scale. The non-local plastic constitutive behavior of the rock, combined with the classical Biot's poroelastic theory, was implemented using a new implicit C^0 non-local finite element method. A predictor-corrector return algorithm for the non-local plasticity model was formulated as an extension of the classical plasticity algorithm. To improve the performance of the iterative solution scheme, a consistent algorithmic stiffness tangent modulus was developed. First, the elastic-plastic constitutive behavior of the proposed methodology is verified using the standard non-porous biaxial compression test with strain softening behavior. Next, it is verified that the poro-elastic-plastic model correctly simulates the evolution of the stimulated zone and the subsequent change in the flow and fluid pressure for several hydraulic fracturing examples under various far-field in-situ stress conditions. Lastly, the non-local poro-elastic-plastic model is shown to be mesh-independent and capable of capturing a wide range of complex fracturing behavior.

1. Introduction

Hydraulic Fracturing (HF) is a common technique used in the oil and gas industry to stimulate production from tight hydrocarbon-bearing formations including coal beds, shales, mudstones, and tight sandstones [1]. Other applications of this technology include the pre-conditioning of massive ore bodies in block caving mining [2, 3],

*Corresponding author. email: rgracie@uwaterloo.ca

Email addresses: esarvaramini@uwaterloo.ca (Erfan Sarvaramini), mauriced@uwaterloo.ca (Maurice B. Dusseault), mohammad.komijani@uwaterloo.ca (Mohammad Komijani), rgracie@uwaterloo.ca (Robert Gracie)

compensation for ground subsidence during tunneling [4], and the disposal of wastes in underground formations [5, 6]. During HF, a fluid slurry is injected into a target formation under high pressure, causing deformation and failure (fracture) of the rock mass and increasing the permeability in a region surrounding the injection point – creating a Stimulated Volume (SV).

The existence of a post-HF zone of globally enhanced permeability (the SV) has been widely recognized in the HF literature [7, 8, 9]. During a typical HF operation in a naturally fractured rock mass, the injected fluid initially creates Mode I tensile fractures that propagate preferentially along the local natural fractures, as they possess far lower fracture toughness than the dense, strong rock matrix [10, 8]. The propagation of tensile fractures can significantly increase the shear stress in the macroscopic vicinity of the fracture tips, at a scale of meters or tens of meters, depending on the fracture aperture and curvature. This, combined with a reduction of the effective confining stress due to increased fluid pressures, leads to shear slip events along the pre-existing fractures intersecting or close to the propagating tensile cracks, effectively bifurcating the crack fronts, increasing fracture network complexity, and leading to irreversible volume changes through shear dilation [8, 9]. As the result, the fracture network can be quite complex on the length scale of the strong local fabric. At a larger scale, however, the SV is aligned with the orientation of the maximum principal stress due to the principle of work minimization [11, 9].

Since the goal of HF is to enhance the permeability of a reservoir, it is useful to think of the SV as being divided into two zones, each in which permeability enhancement is dominated by a different mechanism. The innermost zone that is closest to the well is mostly dominated by Mode I tensile fracture deformation, and is called the "sand zone" because it is the zone that cane be most easily propped by injected sand (Fig. 1a) [8, 9]. Beyond the sand zone is the shear dilation zone, in which deformation is dominated by shear and slip events of Mode II and Mode III nature , as evidenced by microseismic imaging [7, 12] (Fig. 1a). Shear fracturing along pre-existing fractures is accompanied by shear dilation, resulting in a zone of naturally propped and more permeable fractures. The shear dilation zone is expected to be much larger than the sand zone and is thought to significantly contribute to permeability enhancement and hence to production from tight reservoirs [7, 8, 9].

It is important to recognize that the naturally fractured fabric of the target formations leads to the creation of the complex fracture networks in a volume of plastically deformed and damaged rock mass, rather than leading to a single conductive fracture [7, 12, 9]. Permanent deformations from the reactivation and shear dilation of natural and induced fractures are required for the creation of a stimulated volume; reversible elasticity processes are insufficient.

The primary contribution of this article is the presentation of a simulation scheme aimed at modeling the SV (i.e., the effective behavior of a network of fractures) created by hydraulic fracturing. The primary focus of convectional HF modeling has been on the simulation of individual hydraulic fractures and their tip processes and asymptotic behaviors [13, 14, 15]. When a group or network of hydraulic fractures is mathematically simulated, it is generally done by explicitly modeling each fracture using discrete fracture models [16, 17]. Whereas previous efforts in non-local plas-

ticity models for porous media have focused application to localization phenomena of individual cracks and shear bands [18, 19], here we used a similar paradigm to model the evolution of a stimulated volume. This allows larger scale (reservoir-scale) problems of hydraulic fracturing to be more readily modeled.

Discontinuum approaches, e.g., the distinct element approach (DEM), treating jointed rock masses as an assemblage of blocks with stipulated contact laws, are commonly used to account for the strong fabric effects on the propagation of hydraulic fractures in naturally fractured rock [20, 21]. The high computational burden for large scale problems, small discretization sizes and explicit time stepping, and the single scale nature of the constitutive laws are among the major drawbacks of discontinuum approaches [22]. This motivates development of more efficient continuum approaches which incorporate the effective behavior of the natural fracture network, making simulation of a wide range of HF processes possible. It has recently been shown that it is possible to accurately parameterize the hardening behavior of the continuum plastic-damage model using triaxial load curves from the representative element volumes DEM simulations [22]. Thus, it is possible to build up-scaled continuum models that are able to, in an average sense, capture the behavior of naturally fractured rock masses. In this article, we present an alternative macroscale continuum approach with the goal of simulating the evolution of the SV during HF.

We assume that the Stimulated Volume in the jointed rock mass can be represented by an equivalent non-local poro-elastic-plastic continuum zone of enhanced permeability. The details of the complex fracturing, nucleation and micro-events of coalescence that occur at the discrete level are not explicitly modeled; instead, their effects are translated into three constitutive models: (1) for the degradation of the yield strength of rock (plastic softening), (2) for the evolution of effective permeability with plasticity, and (3) for the energy dissipation within the localization band, which is controlled by an internal characteristic length scale,ℓ_c, that is related to the natural fracture distribution and spacing as well as the micromechanics of deformation. Note that in this study, we assume that the group of natural fractures (when subjected to the confining stress and pore fluid loading) tends to predominantly exhibit plastic softening behavior and plastic hardening stage is neglected. This assumption can be true for a network of fractures in which the micro- cracking and void coalescence of the fracture network at the discrete level will lead to the progressive degradation of the material cohesion.

The idea of a non-local plastic softening model for the jointed rocks in this article is inspired in part by the classical strain localization and shear band propagation modeling in dry [23, 24] and saturated geomaterials [18, 19] in application to the problems in geotechnical engineering. The strain localization band is a zone of intense shearing and inelastic deformation that forms during the plastic-softening stage [25]. The thickness of this zone is controlled by the microstructure and has been previously characterized by Bažant and Oh [26]. In this article, we extend the non-local plasticity theory to model the SV in porous jointed rocks.

In previous non-local plasticity models for saturated porous media, e.g., [18, 19], localization was driven by mechanical loading on the domain boundaries. This is in contrast to the creation of the stimulated volume in hydraulic fracturing applications

which is driven by pore fluid injection and the initial in-situ stress field. This significant difference in loading type, results in unique phenomena, which have not yet explored in the literature of non-local plasticity.

In this article, we extend the non-local plasticity theory to model the SV in porous jointed rocks. The mechanism of shear band localization in geotechnical applications is primarily due to the mechanical loading enforced as traction forces on the domain boundaries. However, the creation of the strain localized band for hydraulic fracturing applications is governed by the diffusion loading which together with the initial in-situ stress field results in certain unique features which have not yet explored in the literature.

Use of non-local and gradient-based plasticity and damage models is often motivated by a desire to overcome the well-known pathological problems of mesh dependence which occur in FEM simulations with classical plasticity and damage models when strain softening occurs [26, 27, 28]. In this article, the introduction of a non-local plasticity model serves the dual purpose of ensuring that the discrete problem remains well-posed while enshrining a length scale associated with the natural fracture fabric into the constitutive model. Note that plasticity models have been used previously in the context of hydraulic fracture simulation e.g., [29, 30, 31]; however, these models have not tied up the post yielding behavior of the softening materials to a characteristic length scale leading to the aforementioned pathological mesh dependence of the numerical results.

A non-local poro-elastic-plastic model is presented and implemented within a Finite Element Method (FEM) framework based on the classical Biot's Theory. Energy dissipation due reactivation of the fracture network and permanent plastic deformation of the poro-elasto-plastic body is achieved though the plastic work. The Drucker-Prager yield criterion [32] is used to incorporate the complex fracture behavior of the fracture network (SV) associated with both tensile softening (Mode I) and and shear dilation (Mode II and III) when stress triaxiality is large. A new implicit C^0 non-local plasticity model is proposed for the non-local plastic constitutive behavior, which is an approximation of C^1 non-local continuity models introduced in [27, 33]. This is achieved by reformulation of the traditional model for the non-local plasticity [34, 35]. The predictor-corrector algorithm for the proposed C^0 model is developed in a manner similar to the classical plasticity theory [36], but differs from the manner in which non-local plasticity is usually implemented. To facilitate the numerical convergence of the governing equations, a consistent algorithmic tangent operator is also derived.

Damage mechanics based smeared fracture models, such as phase field models [37, 38] and the non-local permeability model [39], have been applied to the HF problem. The phase field approach fails to account for permeability enhancement from permanent/plastic shear dilation and thus cannot be used to quantify the zone of shear dilation. Furthermore, this approach does not tie the length scale that appears in those models with the characteristic lengths of the natural fracture network or microstructure of the rock mass. Rather, there has been a lot of effort dedicated to showing that phase field models converge to linear elastic fracture mechanics solutions in the limit as the length-scale goes to zero [40]. The non-local permeability method [39] is a new approach inspired from the non-local transport theory [41, 42] which

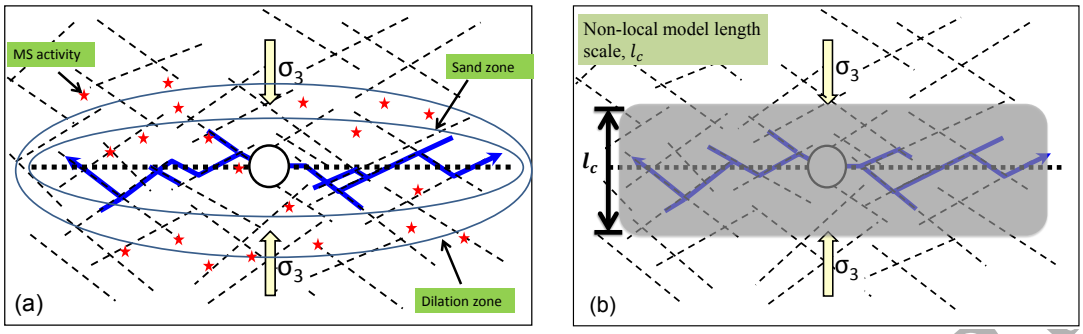

Figure 1: (a) The various stimulated zones during injection into a naturally fractured system [9]. (b) Equivalent continuum approximation of the stimulated zone controlled by the length scale l_c.

defines a characteristic length scale for the flow (permeability). This approach seems promising, but like other purely damage approaches does not incorporate the effect of permanent shear dilation, and hence the related permeability enhancement from plastic shear dilation. A realistic representation of the SV should account for both degradation of the elastic modulus (i.e., damage) and the yield strength (plasticity). In this study, the effect of damage and elastic degradation on the strain localization is neglected for the sake of simplicity; it will be addressed in the future.

This paper is organized as follows. In Sec. 2, the problem setting and governing equations are presented. The numerical implementation and procedure are discussed in Sec. 3. The effectiveness of the proposed model is demonstrated for a series of fracturing propagation examples in Sec. 4.

2. Mathematical formulation

Consider a poro-elasto-plastic body in the domain $\Omega \in R^2$ bounded by $\partial\Omega$ (Fig. 2). The boundary $\partial\Omega$ is composed of the sets of prescribed displacements $\partial\Omega_u$, traction $\partial\Omega_t$, flow rate $\partial\Omega_q$, pressure $\partial\Omega_p$ and plastic $\partial\Omega_\varrho$ boundaries such that $\partial\Omega_u \cup \partial\Omega_t = \partial\Omega_q \cup \partial\Omega_p = \partial\Omega$ and $\partial\Omega_u \cap \partial\Omega_t = \partial\Omega_q \cap \partial\Omega_p = \emptyset$. The domain Ω is further decomposed into an elastic domain Ω_e and a plastic domain Ω_ϱ. The behavior of the body subjected to the given boundary conditions is described by the following equations:

2.1. Non-local constitutive behavior of the rock matrix

Hooke's law

The elasto-plastic constitutive behavior of the rock matrix due to an external loading is described by the generalized Hooke's law

$$\Delta\boldsymbol{\sigma}' = \boldsymbol{C} : \Delta\boldsymbol{\varepsilon}^e, \tag{1}$$

where $\Delta\boldsymbol{\sigma}'$ and $\Delta\boldsymbol{\varepsilon}^e$ are the increments in the effective stress and elastic strain tensors, respectively, and $\boldsymbol{C}$ is the fourth-order stiffness tensor.

The material subjected to an increasing load may yield when the load on the material exceeds the elastic limit. At this point, the material will experience elastic

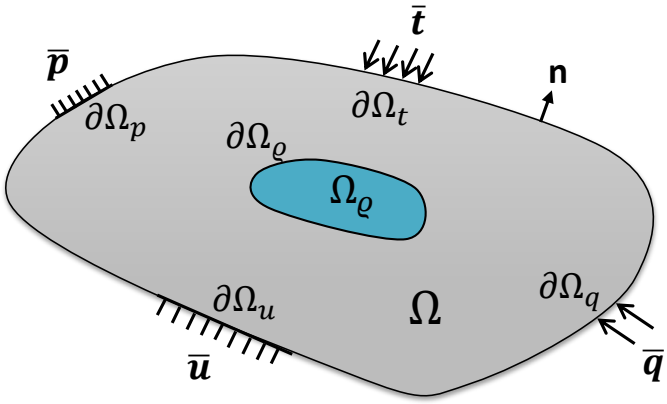

Figure 2: Schematic of the problem domain.

and plastic strains. The elastic component of the strain increment tensor can be expressed in terms of the total strain $\Delta\boldsymbol{\varepsilon}$ and plastic strain $\Delta\boldsymbol{\varepsilon}^p$ increment tensors as:

$$\Delta\boldsymbol{\varepsilon}^e = \Delta\boldsymbol{\varepsilon} - \Delta\boldsymbol{\varepsilon}^p. \tag{2}$$

The total strain can be defined in terms of the symmetric part of the displacement gradient strain tensor given by:

$$\boldsymbol{\varepsilon} = \frac{1}{2}(\nabla\boldsymbol{u} + \nabla\boldsymbol{u}^T), \tag{3}$$

in which $\boldsymbol{u}(\boldsymbol{x})$ denotes the displacement and $\boldsymbol{x} \in \Omega$ is a material point.

Associated flow rule

The amount of plastic strain can be obtained from the plastic flow rule. The general form of the associated flow rule is given by [43]

$$\Delta\boldsymbol{\varepsilon}^p = \Delta\lambda\frac{\partial f}{\partial\boldsymbol{\sigma}'}, \tag{4}$$

where λ is the plastic multiplier and f is a particular yield function. Since the plastic multiplier is a scalar quantity, the plastic strain rate is directed outward from the plastic yield surface.

In this study, we use the associated flow rule with the Drucker-Prager (DP) yield criterion. The DP failure criterion is widely used to study the failure behavior of geomaterials, e.g., rocks, concrete, and soil. The DP yield function is given by [32]

$$f\left(\boldsymbol{\sigma}', \tilde{e}^p\right) = \left(\boldsymbol{s}'_{ij}\boldsymbol{s}'_{ij}\right)^{1/2} + \sqrt{\frac{2}{3}}\alpha_f\boldsymbol{\sigma}'_{\boldsymbol{m}} - \sqrt{\frac{2}{3}}\beta\sigma_y(\tilde{e}^p). \tag{5}$$

Here, $\boldsymbol{s}'$ denotes the deviatoric effective stress tensor, α_f and β are positive constants relating to the material properties, $\boldsymbol{\sigma}'_m$ is the volumetric effective stress, and

σ_y is the yield stress expressed as a function of the non-local equivalent plastic strain $\tilde{e}^p$. Note that the special case of the Von Mises failure criterion can be obtained from (5) by letting $\alpha_f = 0$ and $\beta = 1$.

For linear isotropic softening materials, the yield stress function takes the form

$$\sigma_y = \sigma_{y0} + h\tilde{e}^p, \tag{6}$$

in which σ_{y0} is the initial yield stress and h is the linear isotropic hardening coefficient which is negative for softening materials (for $h < 0$) .

The incremental form of the non-local equivalent plastic strain can be written as [24]

$$\Delta\tilde{e}^p = \Delta e^p + c\nabla^2\Delta e^p + \frac{3}{10}c^2\nabla^4\Delta e^p + \cdots . \tag{7}$$

Here, Δe^p is the corresponding local plastic strain increment counterpart and $c = (l_c^2/24)$ is a coefficient related to the non-local plastic length scale l_c. Note that the classical local plasticity theory can be recovered from (7) by letting $c \approx 0$. Neglecting the fourth-order term in (9) leads to well-known explicit gradient formulation for elasto-plasticty [28]

$$\Delta\tilde{e}^p = \Delta e^p + c\nabla^2\Delta e^p. \tag{8}$$

Differentiation of (8) twice and substituting the result back into equation (8) gives

$$\Delta\tilde{e}^p - c\nabla^2\Delta\tilde{e}^p = \Delta e^p - c^2\nabla^4\Delta e^p. \tag{9}$$

The equation can be further simplified to:

$$\Delta\tilde{e}^p - c\nabla^2\Delta\tilde{e}^p = \Delta e^p, \tag{10}$$

referred to as the implicit-gradient formulation for elasto-plasticty [34].

The additional condition on the non-local boundary of the plastic domain is given by [34]:

$$\boldsymbol{n}_{\varrho} \cdot \nabla\Delta\tilde{e}^p \big|_{\partial\Omega_{\varrho}} = 0, \tag{11}$$

where $\boldsymbol{n}_{\boldsymbol{\varrho}}$ is the unit normal vector pointing outward from the plastic boundary surface. Note that the boundary condition (10) assumes that the traction vanishes at the moving boundary of the plastic domain.

The local effective plastic strain increment in (10) can be obtained by the well-known expression

$$\Delta e^p = \sqrt{\frac{2}{3}\Delta\boldsymbol{\varepsilon}^p : \Delta\boldsymbol{\varepsilon}^p}, \tag{12}$$

which for the DP yield criterion can be expressed as [33]

$$\Delta e^p = \sqrt{\frac{2}{3}(1 + \frac{2}{9}\alpha^2)}\Delta\lambda. \tag{13}$$

2.2. Non-local constitutive behavior of flow

The flow of the fluid through the porous medium is described by the Darcy's law given by

$$\boldsymbol{q} = -\frac{k\left(\tilde{e}^p\right)}{\mu}\nabla p, \tag{14}$$

where $\boldsymbol{q}$ is the fluid discharge tensor, μ is the viscosity of the fluid, and k is the permeability of the porous medium assumed to be a function of the non-local equivalent plastic strain $\tilde{e}_p$.

One may express the permeability k as a Taylor series expansion in $\tilde{e}^p$ as

$$k\left(\tilde{e}_p\right) = k|_{\tilde{e}^p=0} + \left.\frac{dk}{d\tilde{e}^p}\right|_{\tilde{e}^p=0}\tilde{e}^p + \frac{1}{2!}\left.\frac{d^2k}{d\tilde{e}_p^2}\right|_{\tilde{e}^p=0}\tilde{e}^{p2} + \ldots \tag{15}$$

Although the derivatives in (15) are unknown, one may seek a solution in the form of an empirical function relating the rock mass permeability to the accumulated plastic strain as

$$k = k_0\left(1 + a\left(\tilde{e}^p\right)^b\right), \tag{16}$$

where k_0 is the initial permeability and $a \geq 0$ and b are constant coefficients to be calibrated.

2.3. Equilibrium equation

The equilibrium equation and boundary conditions for the system described in Fig. 1 are

$$\nabla \cdot (\boldsymbol{\sigma}' - \alpha p \boldsymbol{I}) = 0, \tag{17}$$

and

$$\boldsymbol{\sigma} \cdot \boldsymbol{n}\,|_{\partial\Omega_t} = \bar{\boldsymbol{t}}, \quad \boldsymbol{u}\,|_{\partial\Omega_u} = \bar{\boldsymbol{u}}, \tag{18}$$

where α is the Biot coefficient, $\boldsymbol{I}$ is the identity tensor, $\boldsymbol{\sigma}$ is the total stress tensor on the boundary surface, $\boldsymbol{n}$ is the unit normal vector perpendicular to the boundary surface, and $\bar{\boldsymbol{t}}$ and $\bar{\boldsymbol{u}}$ are the prescribed traction and displacement tensors on the boundaries $\partial\Omega_t$ and $\partial\Omega_u$, respectively. Note that inertia and body forces are neglected in (17).

2.4. Continuity equation for the fluid phase

Applying the law of conservation of mass leads to the local continuity equation

$$\frac{\partial\zeta}{\partial t} + \nabla \cdot \boldsymbol{q} = 0, \tag{19}$$

where ζ is the fluid content. The constitutive law relating the fluid content ζ and pressure p is expressed as

$$p = M(\zeta - \alpha \mathbf{tr}(\boldsymbol{\varepsilon})). \tag{20}$$

Here, M is the Biot modulus and $\mathbf{tr}(\boldsymbol{\varepsilon}) = \varepsilon_V$ is the trace of the strain tensor. The sets of initial and boundary conditions corresponding to the flow equation (19) are

$$p\,|_{t=0} = p_0, \quad \boldsymbol{n}\cdot\boldsymbol{q}\,\big|_{\partial\Omega_q} = \overline{q} \quad p\,\big|_{\partial\Omega_p} = \bar{p}, \tag{21}$$

where p_0 is the initial pore pressure and $\overline{q}$ and $\bar{p}$ are the prescribed flow rate and pressure on the boundaries $\partial\Omega_q$ and $\partial\Omega_p$, respectively. Substitution of ζ from (20) in (19) and rearranging the result gives

$$\frac{1}{M}\frac{\partial p}{\partial t} + \alpha\frac{\partial \varepsilon_V}{\partial t} - \frac{1}{\mu}\nabla\cdot\left(k\left(\tilde{e}^p\right)\nabla p\right) = 0. \tag{22}$$

3. Numerical implementation

The summary of the set of governing equations and corresponding boundary conditions to describe the behavior of the body described in Fig. 1 are:

- Equilibrium
$$\nabla\cdot(\boldsymbol{\sigma}' - \alpha p\boldsymbol{I}) = 0,\ \boldsymbol{x}\in\Omega \tag{23}$$
- Non-local plasticity
$$\Delta\tilde{e}^p - c\nabla^2\Delta\tilde{e}^p = \Delta e^p,\ \boldsymbol{x}\in\Omega_\varrho \tag{24}$$
- Fluid flow
$$\frac{1}{M}\frac{\partial p}{\partial t} + \alpha\frac{\partial \varepsilon_V}{\partial t} - \nabla\cdot\left(\frac{k}{\mu}\nabla p\right) = 0,\ \boldsymbol{x}\in\Omega \tag{25}$$
- Initial and boundary condition
$$p\,|_{t=0} = p_0,\ \boldsymbol{n}.\boldsymbol{q}\,\big|_{\partial\Omega_q} = \bar{q},\ p\,\big|_{\partial\Omega_p} = \bar{p},\ \boldsymbol{\sigma}.\boldsymbol{n}\,|_{\partial\Omega_t} = \bar{\boldsymbol{t}},\ \boldsymbol{u}\,|_{\partial\Omega_u} = \bar{\boldsymbol{u}},\ \boldsymbol{n}_{\boldsymbol{\varrho}}\cdot\nabla\Delta\tilde{e}^p\,\big|_{\partial\Omega_\varrho} = 0. \tag{26}$$

The weak formulation of the system of governing equations is obtained in the standard way. We choose three arbitrary weight functions $\boldsymbol{w_u}$, w_ϱ, w_p for the displacement $\boldsymbol{u}$, non-local plastic strain increment $\Delta\tilde{e}^p$, and pressure p fields, respectively. The weak form of the governing equations (23-25) after applying the boundary conditions (26) for the sets of $\boldsymbol{u}\in U^0$, $\triangle\tilde{e}^p\in\varrho^0$, and $p\in P^0$ can be written as

$$\int_\Omega \nabla\boldsymbol{w_u} : (\boldsymbol{\sigma}' - \alpha p\boldsymbol{I})d\Omega = \int_{\partial\Omega_t}\boldsymbol{w_u}\cdot\bar{\boldsymbol{t}}d\Gamma,\ \forall\boldsymbol{w_u}\in U^0 \tag{27}$$

$$\int_{\Omega_\varrho} w_\varrho\Delta\tilde{e}^p d\Omega + c\int_{\Omega_\varrho}\nabla w_\varrho^T\cdot\nabla\Delta\tilde{e}^p d\Omega = \int_{\partial\Omega_\varrho} w_\varrho^T\Delta e^p d\Gamma,\ \forall w_\varrho\in\varrho^0 \tag{28}$$

$$\frac{1}{M}\int_\Omega w_p\frac{\partial p}{\partial t}d\Omega + \alpha\int_\Omega w_p\frac{\partial\varepsilon_V}{\partial t}d\Omega + \frac{1}{\mu}\int_\Omega\nabla w_p\cdot k\left(\tilde{e}^p\right)\nabla p d\Omega = \int_{\partial\Omega_p} w_p\bar{q}d\Gamma,\ \forall w_p\in P^0. \tag{29}$$

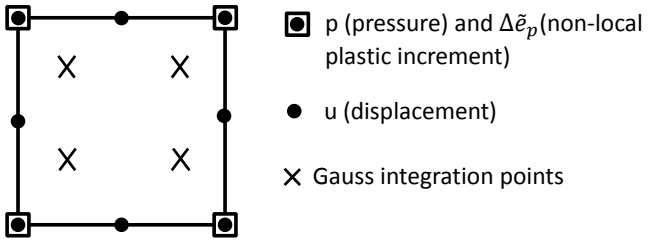

Figure 3: Schematic of the mixed finite element. The 8-node serendipity elements for displacement and 4-node linear element for the pressure and non-local plastic strain increment are used for numerical calculations.

3.1. Semi-discrete and discrete equations

We first discretize $\boldsymbol{u}$, p and $\Delta\tilde{e}^p$ using a mixed finite element, as illustrated in Fig. 3.

The displacement $\boldsymbol{u}(\mathbf{x},t)$, pressure $p(\mathbf{x},t)$, and non-local plastic strain increment $\Delta\tilde{e}^p(\mathbf{x},t)$ are approximated as

$$\boldsymbol{u}(\boldsymbol{x},t)=\sum_{\forall I\in S^u} N_I^u(\boldsymbol{x})u_I(t),\quad \Delta\tilde{e}^p=\sum_{\forall I\in S^\varrho} N_I^\varrho(\boldsymbol{x})\Delta\tilde{e}_I^p(t),\quad p(\boldsymbol{x},t)=\sum_{\forall I\in S^p} N_I^p(\boldsymbol{x})p_I(t), \tag{30}$$

respectively, in which N_I^u, N_I^ϱ, N_I^p are the standard finite element shape functions used to interpolate the displacements, non-local plastic strain increment, and pore pressure fields. S^u, S^p, and S^ϱ are the sets of node I for the $\boldsymbol{u}$, p, and $\Delta\tilde{e}^p$ approximations, respectively. Let the displacements, non-local plastic strain increment, and pressure degrees of freedom vectors be $\mathbf{d}^u=\{\boldsymbol{u}_1,\boldsymbol{u}_2,\ldots\}^\top$, $\mathbf{d}^\varrho=\{\Delta\tilde{e}_1^p,\Delta\tilde{e}_2^p,\ldots\}^\top$, and $\mathbf{d}^p=\{p_1,p_2,\ldots\}^\top$, and their respective time derivatives be $\dot{\mathbf{d}}^u$, $\dot{\mathbf{d}}^\varrho$, and $\dot{\mathbf{d}}^p$. The mixed nature of the system of equations (27-29) requires the selection of suitable shape functions for the pore pressure, displacement and non-local plastic strain increment fields to satisfy the LBB stability condition [44]. This is achieved by selecting 8-node quadrilateral shape functions for displacement and 4-node bi-linear shape functions for pore pressure and the non-local plastic strain increment.

Substitution of (30) into the weak forms (27-29) and applying the standard divergence theorem leads to the following semi-discrete equations

$$\boldsymbol{R}^u(\boldsymbol{d}^u,\boldsymbol{d}^\varrho,\boldsymbol{d}^p)=\int_\Omega \boldsymbol{B}^{uT}\{\boldsymbol{\sigma}'\}\,d\Omega-\int_\Omega \boldsymbol{B}^{uT}\alpha\underset{1\times 3}{\bar{\boldsymbol{I}}}pd\Omega-\int_{\partial\Omega_t}\boldsymbol{N}^{pT}\bar{\boldsymbol{t}}d\Gamma=\mathbf{0} \tag{31}$$

$$\boldsymbol{R}^\varrho(\boldsymbol{d}^u,\boldsymbol{d}^\varrho,\boldsymbol{d}^p)=\int_{\Omega_\varrho}\boldsymbol{N}^{\varrho T}\Delta\tilde{e}^p d\Omega+\int_{\Omega_\varrho}\boldsymbol{B}^{\varrho T}c\nabla\Delta\tilde{e}^p d\Omega-\int_{\Omega_\varrho}\boldsymbol{N}^{\varrho T}\Delta e^p d\Omega=\mathbf{0} \tag{32}$$

$$\boldsymbol{R}^p(\boldsymbol{d}^u,\boldsymbol{d}^\varrho,\boldsymbol{d}^p)=\frac{1}{M}\int_\Omega \boldsymbol{N}^{pT}\dot{p}d\Omega+\alpha\int_\Omega \boldsymbol{N}^{pT}\dot{\epsilon}_V d\Omega-\int_\Omega \boldsymbol{B}^{pT}\frac{k\left(\tilde{e}^p\right)}{\mu}\nabla p d\Omega-\int_{\partial\Omega_p}\boldsymbol{N}^{pT}\bar{q}d\Gamma=\mathbf{0}. \tag{33}$$

Here, $\boldsymbol{B}^u$ is the standard B-matrix of shape function derivatives for an 8-node quadrilateral element for displacements, $\boldsymbol{B}^p$ and $\boldsymbol{B}^\varrho$ are the standard B-matrices for a

4-node quadrilateral element for scalar fields, $\boldsymbol{N}^u$, $\boldsymbol{N}^p$, and $\boldsymbol{N}^\varrho$ are the corresponding matrices of shape functions, $\{\boldsymbol{\sigma}'\}$ denotes the effective stress in Voigt form, and $\underset{1\times3}{\bar{\boldsymbol{I}}} = \begin{bmatrix} 1 & 1 & 0 \end{bmatrix}^\top$.

We will solve (31-33) using a fixed point iterative scheme by first solving simultaneously for $\boldsymbol{d}^u$ and $\boldsymbol{d}^p$ and then solving for $\boldsymbol{d}^\varrho$ and iterating until convergence. To this end let the solution vector $\boldsymbol{d}$ and a residual vector $\boldsymbol{R}$ be given respectively as:

$$\boldsymbol{d} = \begin{bmatrix} \mathbf{d}^u \\ \mathbf{d}^p \end{bmatrix}, \qquad \boldsymbol{R} = \begin{bmatrix} \mathbf{R}^u \\ \mathbf{R}^p \end{bmatrix}. \tag{34}$$

Let $\boldsymbol{d}^n$ and $\boldsymbol{d}^{n+1}$ be the values of $\boldsymbol{d}$ at times t_n and t_{n+1}, respectively, and let the time step size be denoted by Δt, such that $t_{n+1} = t_n + \Delta t$. Let the time derivatives of $\dot{\mathbf{d}}^u$ and $\dot{\mathbf{d}}^p$ be approximated using a backwards Euler scheme of the form:

$$\dot{\boldsymbol{d}}^{n+1} = \frac{1}{\Delta t}\left(\boldsymbol{d}^{n+1} - \boldsymbol{d}^n\right) \tag{35}$$

Substitution of (35) into (31-33) yields a non-linear system of equations for $\boldsymbol{d}^{n+1}$, which is solved by linearizing (34). Let $\mathbf{d}_i^{n+1}$ be the solution at iteration i of time t_{n+1}. Let the increment in the solution from one iteration to the next be denoted by $\Delta\mathbf{d}_i$ and given by $\mathbf{d}_{i+1}^{n+1} = \mathbf{d}_i^{n+1} + \Delta\mathbf{d}_i$. At iteration $i+1$ of the NR solver, the following linear system of equations is solved

$$\left(\frac{1}{\Delta t}\boldsymbol{M} + \boldsymbol{K}\left(\mathbf{d}_i^{n+1}\right)\right)\Delta\boldsymbol{d}_i = -\boldsymbol{R}\left(\mathbf{d}_i^{n+1}\right). \tag{36}$$

The components of the tangent stiffness matrix are:

$$\boldsymbol{K}_{uu} = \int_\Omega \boldsymbol{B}^{uT}\boldsymbol{C}^{alg.}\boldsymbol{B}^u d\Omega, \tag{37}$$

$$\boldsymbol{K}_{up} = -\int_\Omega \boldsymbol{B}^{uT}\alpha\,\underset{1\times3}{\bar{\boldsymbol{I}}}\,\boldsymbol{N}^p d\Omega,$$

$$\boldsymbol{K}_{pp} = \int_\Omega \boldsymbol{B}^{pT}\frac{k(\tilde{e}^p)}{\mu}\boldsymbol{B}^p d\Omega,$$

$$\boldsymbol{M}_{pu} = \int_\Omega \boldsymbol{N}^{pT}\alpha\boldsymbol{B}^{uT,vol} d\Omega,$$

$$\boldsymbol{M}_{pp} = \int_\Omega \boldsymbol{N}^{pT}\frac{1}{M}\boldsymbol{N}^p d\Omega,$$

$$\boldsymbol{K}_{pu} = \boldsymbol{M}_{uu} = \boldsymbol{M}_{up} = 0, \tag{38}$$

Here, $\boldsymbol{C}^{alg.}$ is the consistent algorithmic stiffness tangent modulus, the derivation of which is described in the next section.

During each load step, a fixed point iteration strategy is used to solve (31)-(33). Starting from an initial value for $\tilde{e}^p$, equations (31) and (33) are solved using the

Newton-Raphson method to find $\boldsymbol{d}^u$ and $\boldsymbol{d}^p$. During the stress update and computation of the consistent algorithmic stiffness tangent modulus, the system of equations (32) is solved for $\boldsymbol{d}^{\varrho}$. The solution of (32) is discussed in the following subsection.

3.1.1. Consistent algorithmic stiffness tangent modulus

The general form of the consistent algorithmic stiffness tangent modulus in matrix form can be expressed as [45]

$$\boldsymbol{C}^{alg.} = \boldsymbol{C} - \boldsymbol{C}\boldsymbol{n_{\varrho}}^T \left(\frac{\partial \Delta\lambda}{\partial \varepsilon_I}\right) - \Delta\gamma \boldsymbol{C} \left(\frac{\partial \boldsymbol{n_{\varrho}}}{\partial \varepsilon_I}\right), \tag{39}$$

in which, $\boldsymbol{C}$ is stiffness matrix of the solid material, and $\boldsymbol{n_{\varrho}}$ is the normal to the yield surface. For the DP yield criterion $\boldsymbol{n_{\varrho}}$ takes the form [33]

$$\boldsymbol{n_{\varrho}} = (\boldsymbol{n_{\varrho D}} + \boldsymbol{n_{\varrho S}}), \tag{40}$$

where $\boldsymbol{n_{\varrho D}} = \left\{\boldsymbol{s}'^e\right\} / \left|\left\{\boldsymbol{s}'^e\right\}\right|$ and $\boldsymbol{n_{\varrho S}} = \sqrt{(2/27)}\alpha \boldsymbol{I}$ are the contributions from deviatoric and spherical parts of the effective stress tensor to $\boldsymbol{n_{\varrho}}$, expressed in terms of bulk modulus K, shear modulus μ, and the elastic part of the deviatoric effective stress $\left\{\boldsymbol{s}'^e\right\}$.

Let us first obtain the expression for $\partial \boldsymbol{n_{\varrho}}/\partial \varepsilon_I$. Taking the derivative of $\boldsymbol{n_{\varrho}}$ with respect to ε_I using (40) yields

$$\frac{\partial \boldsymbol{n_{\varrho}}}{\partial \varepsilon_I} = \frac{\partial \boldsymbol{n_{\varrho D}}}{\partial \varepsilon_I}, \tag{41}$$

and

$$\frac{\partial \boldsymbol{n_{\varrho D}}}{\partial \varepsilon_I} = \frac{\partial}{\partial \varepsilon_I}\left(\frac{\left\{\boldsymbol{s}'^e\right\}}{|\left\{\boldsymbol{s}'^e\right\}|}\right) = \frac{2\mu}{|\left\{\boldsymbol{s}'^e\right\}|}(\boldsymbol{I}_{dev} - \boldsymbol{n_{\varrho D}}^T \boldsymbol{n_{\varrho D}}), \tag{42}$$

in which $\boldsymbol{I}_{dev}$ is the deviatoric identity matrix. Note that (42) is identical to the equivalent expression in the classical plasticity problem.

We use the yield condition (5) to obtain $\partial \Delta\gamma/\partial \varepsilon_I$. The yield condition states that the stress at the point of yielding is required to remain on the yield surface (i.e., $f = 0$). Recall from classical plastic theory that

$$\left|\left\{\boldsymbol{s}'\right\}\right| = \left|\left\{\boldsymbol{s}'^e\right\}\right| - 2G\Delta\lambda, \quad |\left\{\boldsymbol{\sigma}'_m\right\}| = |\left\{\boldsymbol{\sigma}'^e_m\right\}| - \sqrt{2}K\alpha\Delta\gamma. \tag{43}$$

Substitution of (43) in (5) and letting $f = 0$ result

$$\Delta\lambda = \frac{f^e - \sqrt{\frac{2}{3}}\beta h \Delta\tilde{e}^p}{\left(2G + \sqrt{\frac{4}{3}}K\alpha^2\right)}. \tag{44}$$

in which

$$f^e = \left|\left\{\boldsymbol{s}'^e\right\}\right| + \sqrt{\frac{2}{3}}\alpha|\left\{\boldsymbol{\sigma}'^e_m\right\}| - \sqrt{\frac{2}{3}}\beta\left(\sigma_{y0} + h\tilde{e}^{p,n}\right). \tag{45}$$

We now take the derivative of (44) with respect to ε_I

$$\frac{\partial \Delta\lambda}{\partial \varepsilon_I} = \frac{1}{\left(2G + \sqrt{\frac{4}{3}} K\alpha^2\right)} \left(\frac{\partial \left|\{\boldsymbol{s}^e\}\right|}{\partial \varepsilon_I} + \sqrt{\frac{2}{3}}\alpha \frac{\partial \left|\left\{\boldsymbol{\sigma}'^e_m\right\}\right|}{\partial \varepsilon_I} - \sqrt{\frac{2}{3}}\beta h \frac{\partial \Delta\tilde{e}^p}{\partial \varepsilon_I} \right)$$

$$= \frac{1}{\left(2G + \sqrt{\frac{4}{3}} K\alpha^2\right)} \left(2G\boldsymbol{n_{\varrho D}} + 3K\boldsymbol{n_{\varrho S}} - \sqrt{\frac{2}{3}}\beta h \frac{\partial \Delta\tilde{e}^p}{\partial \varepsilon_I} \right). \tag{46}$$

In the above expression, $\partial \Delta\tilde{e}^p / \partial \varepsilon_I$ is unknown and it has yet to be determined. Combining (44) and (13) and substituting the resulting expression in (32) allows one to find the non-local plastic strain increment as

$$\Delta\tilde{e}^p = \boldsymbol{K^{-1}_{\varrho\varrho}} \boldsymbol{F_\varrho}, \tag{47}$$

where

$$\boldsymbol{K_{\varrho\varrho}} = \int_{\Omega_\varrho} \boldsymbol{N^{\varrho T}} m \boldsymbol{N^\varrho} d\Omega + \int_{\Omega_\varrho} \boldsymbol{B^{\varrho T}} c \boldsymbol{B^\varrho} d\Omega,$$

$$m = 1 + \frac{\beta h \sqrt{\frac{4}{9}(1 + \frac{2}{9}\alpha^2)}}{2G + \sqrt{\frac{4}{3}} K\alpha^2}, \tag{48}$$

$$\boldsymbol{F_\varrho} = \frac{\sqrt{\frac{2}{3}(1 + \frac{2}{9}\alpha^2)}}{2G + \sqrt{\frac{4}{3}} K\alpha^2} \int_{\Omega_\varrho} \boldsymbol{N^{\varrho T}} f^e d\Omega. \tag{49}$$

Taking the derivative of (47) with respect to ε_I yields

$$\frac{\partial \Delta\tilde{e}^p}{\partial \varepsilon_I} = \boldsymbol{K^{-1}_{\varrho\varrho}} \frac{\partial \boldsymbol{F_\varrho}}{\partial \varepsilon_I} \tag{50}$$

$$\frac{\partial \Delta\tilde{e}^p}{\partial \varepsilon_I} = \frac{\sqrt{\frac{2}{3}(1 + \frac{2}{9}\alpha^2)}}{2G + \sqrt{\frac{4}{3}} K\alpha^2} \boldsymbol{K^{-1}_{\varrho\varrho}} \int_{\Omega_\varrho} \boldsymbol{N^{\varrho T}} \frac{\partial f^e}{\partial \varepsilon_I} d\Omega, \tag{51}$$

$$\frac{\partial \Delta\tilde{e}^p}{\partial \varepsilon_I} = \frac{\sqrt{\frac{2}{3}(1 + \frac{2}{9}\alpha^2)}}{2G + \sqrt{\frac{4}{3}} K\alpha^2} \boldsymbol{K^{-1}_{\varrho\varrho}} \int_{\Omega_\varrho} \boldsymbol{N^{\varrho T}} \left(2\mu \boldsymbol{n_{\varrho D}} + 3K \boldsymbol{n_{\varrho S}}\right) d\Omega. \tag{52}$$

Substitution of (42), (46) and (52) in (39) yields

$$\boldsymbol{C}^{alg.} = \boldsymbol{C} - \frac{1}{\left(2G + \frac{4}{3} K\alpha^2\right)} \left(2G\boldsymbol{n_{\varrho D}} + 3K\boldsymbol{n_{\varrho S}}\right)^T \left(2\mu \boldsymbol{n_{\varrho D}} + 3K\boldsymbol{n_{\varrho S}} - \right.$$

$$\left. \frac{\beta h \sqrt{\frac{4}{9}(1 + \frac{2}{9}\alpha^2)}}{2G + \sqrt{\frac{4}{3}} K\alpha^2} \boldsymbol{K^{-1}_{\varrho\varrho}} \int_{\Omega_\varrho} \boldsymbol{N^{\varrho T}} \left(2\mu \boldsymbol{n_{\varrho D}} + 3K \boldsymbol{n_{\varrho S}}\right) d\Omega \right) - \frac{4\mu^2 \Delta\gamma}{\left|\{\boldsymbol{s}'^e\}\right|} (I_{dev} - \boldsymbol{n^T_{\varrho D}} \boldsymbol{n_{\varrho D}}). \tag{53}$$

Note that a similar expression for $\partial \Delta\tilde{e}^p / \partial \varepsilon_I$ in the context of explicit non-local plasticity using the Von-Mises failure criterion was derived in [46].

3.2. Stress update procedure

The stress update involves elastic predictor and plastic corrector stages, which are modified to account for non-local plasticity. We initially assume that the initial state of the system at time step t_n is known and the initial variables at the load step n are $\left\{\boldsymbol{\sigma}^{'}\right\} = \left\{\boldsymbol{\sigma}^{'n}\right\}$, $p = p^n$, $\tilde{e}^p = \tilde{e}^{p,n}$. The current iteration for a given time step is denoted by $i = 1, 2, \ldots$.

3.2.1. Predictor step

The summary of the algorithm for the predictor step is as follows:

Step 1. At the current iteration i , $\boldsymbol{\Delta u}_i$ is given

Step 2. Since the stress state at i is unknown, the loading step is assumed to be elastic:

$$\left\{\boldsymbol{\sigma}_i^{'e}\right\} = \left\{\boldsymbol{\sigma}^{'n}\right\} + \left\{\Delta\boldsymbol{\sigma}_i^{'}\right\} = \left\{\boldsymbol{\sigma}^{'n}\right\} + \boldsymbol{C}\Delta\boldsymbol{\varepsilon}_i^e \tag{54}$$

where $\left\{\boldsymbol{\sigma}^{'e}\right\}$ is the elastic effective stress.

Step 3. The DP yield criterion is calculated using the elastic effective stress obtained in step 2:

$$f^e = \left|\left\{\boldsymbol{s}_i^{'e}\right\}\right| + \sqrt{\frac{2}{3}}\alpha|\left\{\boldsymbol{\sigma}_{m,i}^{'e}\right\}| - \sqrt{\frac{2}{3}}\beta\left(\sigma_{y0} + h\tilde{e}^{p,n}\right). \tag{55}$$

Step 4. Check whether the elastic effective stress lies inside ($f^e < 0$) or on/outside ($f^e \geq 0$) of the initial yield surface, i.e., If $f^e < 0$, the state of the stress is elastic:

$$\left\{\boldsymbol{\sigma}^{'n+1}\right\} = \left\{\boldsymbol{\sigma}_i^{'e}\right\}, \tilde{e}^{p,n+1} = \tilde{e}^{p,n}. \tag{56}$$

If $f^e > 0$, the load step at iteration i is plastic and the corrector step must be employed.

Corrector step

When the elastic effective stress from the predictor step lies outside of the yield surface, the elastic increment includes plastic strain and the elastic stress must be corrected as

$$\left\{\boldsymbol{\sigma}_i^{'}\right\} = \left\{\boldsymbol{\sigma}_i^{'e}\right\} - \boldsymbol{C}\Delta\boldsymbol{\varepsilon}_i^p, \tag{57}$$

where the plastic strain increment $\Delta\boldsymbol{\varepsilon}^p$ is given by the associated flow rule (4) as

$$\Delta\boldsymbol{\varepsilon}_i^p = \Delta\lambda(2G\boldsymbol{n}_{\boldsymbol{\varrho D},i} + 3K\boldsymbol{n}_{\boldsymbol{\varrho S},i}). \tag{58}$$

The values of the tensors $\boldsymbol{n}_{\boldsymbol{\varrho D}}$ and $\boldsymbol{n}_{\boldsymbol{\varrho S}}$ are known from the predictor procedure. The only unknown expression in (58) is $\Delta\lambda$ which can be obtained from (44). The corrector solution procedure is as follows:

Step 1. Using the elastic stress obtained in the predictor step, calculate $\Delta\tilde{e}_i^p$ from (47).

Step 2. Interpolate $\Delta\tilde{e}_i^p$ at the Gauss points and calculate $\Delta\gamma_i$ from (44).

Step 3. Calculate the plastic strain tensor from (58).

Step 4. Update stress from (57).

Step 5. Update the non-local plastic strain $\tilde{e}_i^p = \tilde{e}^{p,n} + \Delta\tilde{e}_i^p$.

Step 6. Calculate the consistent algorithmic stiffness tangent (53).

Step 7. Calculate the residuals (36) and check for convergence.

Step 8. If not converged, calculate the stiffness tangent matrix and solve for the new increments using (36).

Step 9. Check the convergence and repeat the iteration $i = i + 1$ until residual in (36) falls below a specific tolerance.

4. Examples

4.1. Dry rock-compression shear band (bench mark)

The study of shear band formation in a standard biaxial compression test using the Von Mises failure criterion is a common exercise in the non-local theory of plasticity. We use this example to validate the elastic-plastic constitutive behavior of the proposed methodology for dry materials.

Consider a rectangular 60mm$\times$120mm block subjected to a uniformly compressive displacement on its upper edge, as illustrated in Fig. 4. The block is deformed under plane strain conditions and porous medium effects are neglected. We assume that the lower edge of the block can move freely in the horizontal direction and is fixed in vertical displacement. In order to prevent rigid body motion, the mid-point of the lower edge is prevented from moving horizontally. In this case, the effective stress prior to the onset of plasticity is uniform throughout the specimen. To facilitate the formation of the shear band, a 100mm^2 defect is introduced in the left corner of the domain by reducing its yield stress by 10%. The material properties used in the study are listed in Table 1 [28].

Shear modulus	$G = 4.0$GPa
Isotropic softening coefficient	$h = -0.4$GPa
Poisson's ratio	$\nu = 0.49$
Initial yield stress	$\sigma_{y0} = 100$MPa
Shear band length scale	$l_c = 3$mm

Table 1: Material properties [28].

The load, in the form of a uniform vertical displacement, d, is applied in a linearly increasing fashion and the total reaction along the top edge of the plate, P, is computed. The resulting load-deflection curves using non-local and local plasticity formulations are illustrated in Fig. 5 for three meshes of 12×24, 24×48, and

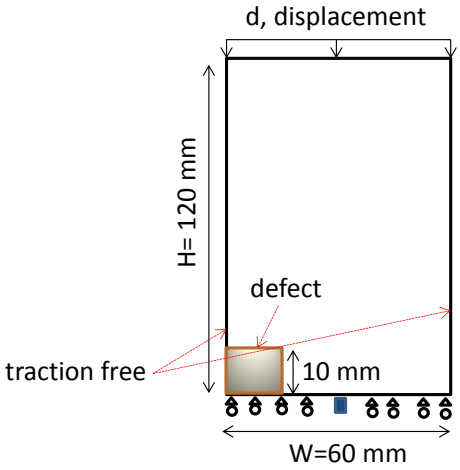

Figure 4: Block schematic for compression shear test.

48×96 mixed rectangular elements. The solution of Pamin [28] obtained using the explicit non-local plasticity model with C^1 continuity is also shown for comparison. As illustrated in Fig. 5, the load initially increases with displacement until strain localization takes place, leading to the reduction in the stress-bearing capacity of the material (i.e.: softening). As the result, the material surrounding the localization band will experience an unloading process.

Load-displacement curves obtained using local plasticity suffer from pathological mesh dependency, which has been extensively discussed in the literature [26, 27, 28]. This problem is circumvented by introducing higher order terms with a characteristic length scale controlling the thickness of the shear band (localization process) in the governing equations. As shown in Fig. 5, the load-displacement curves for the 24×48, and 48×96 element meshes using the non-local plasticity formulation are nearly identical, showing that the localization process is mesh-independent. The convergence of the non-local equivalent plastic strain for a given displacement is also shown in Fig. 6.

It is noted that the non-local model introduced in this paper is C^0 implicit and is different from the C^1 continuity explicit model of Pamin [28]. The evolution equations for the non-local plastic strain in the C^0 continuity (10) and C^1 continuity (8) formulations are different (additional fourth-order term in (9) is neglected), leading to different manifestations of the internal length scale in the results. However, the load-deflection curve for our C^0 continuity implicit formulation with a length scale of 8 mm agrees very well those of the C^1 continuity explicit formulation with a length scale of 3 mm. This example explains that comparable results can be obtained with both formulations, provided that a suitable length scale is used with each. The internal length scale is often associated with micro-crack initiation and void coalescence in the localized zone and has been previously characterized [26]; however, in practice one may use the internal length scale to calibrate the energy dissipation and softening behavior of the model from experimental or field data.

The effect of the length scales of 2mm, 3mm, and 4mm on the load-displacement

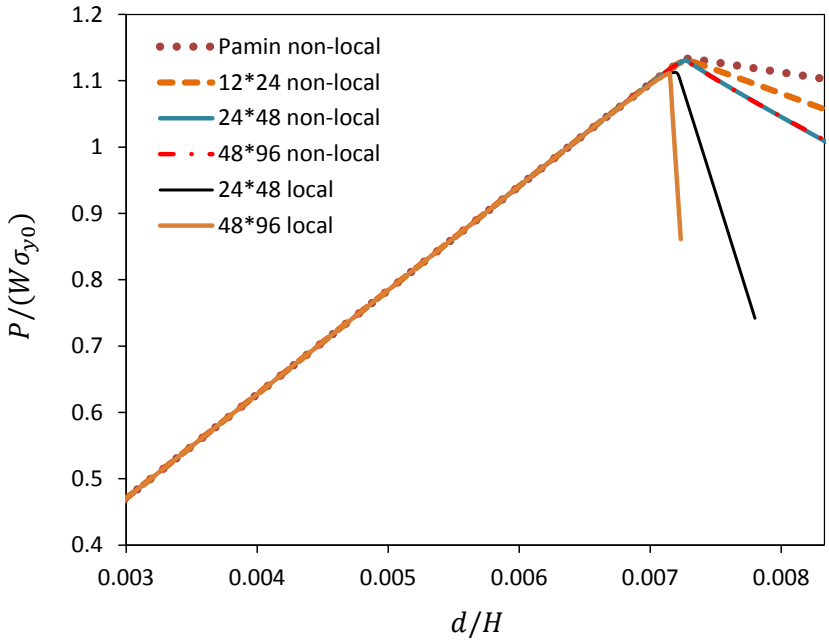

Figure 5: Normalized reaction force $P/(W\sigma_{y0})$ versus normalized displacement d/H for various mesh sizes. Length scale is $l_c = 3$mm.

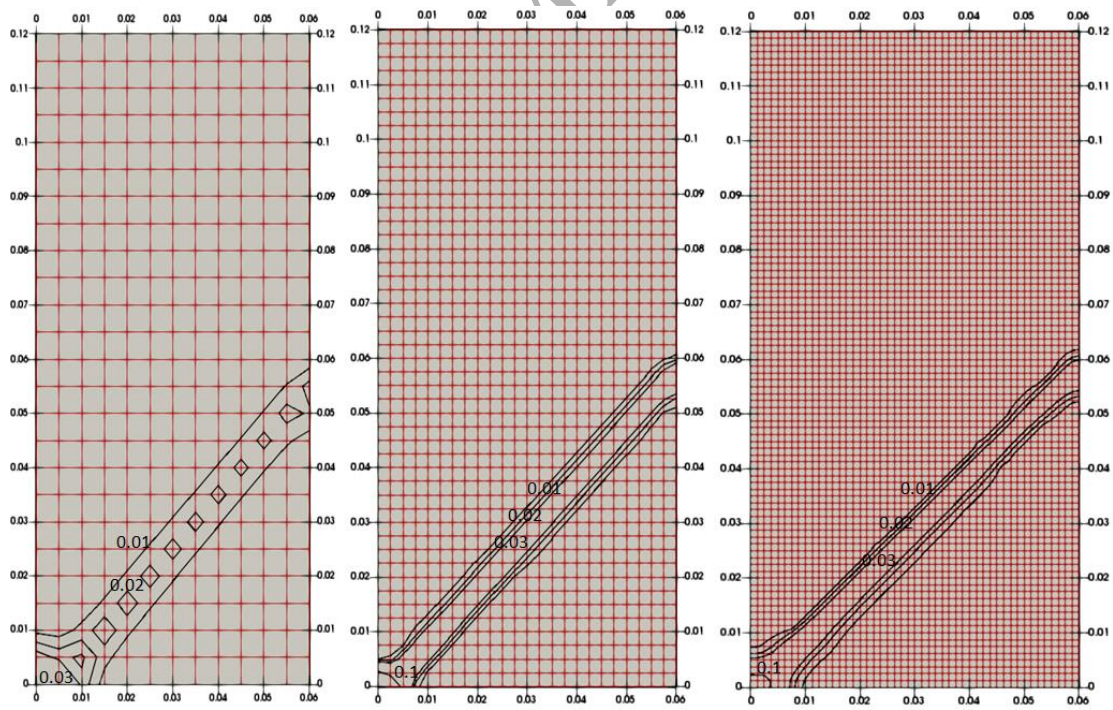

Figure 6: Non-local plastic strain contours for 12×24, 24×48, and 48×96 grids at the given displacement $d/H = 0.0083$.

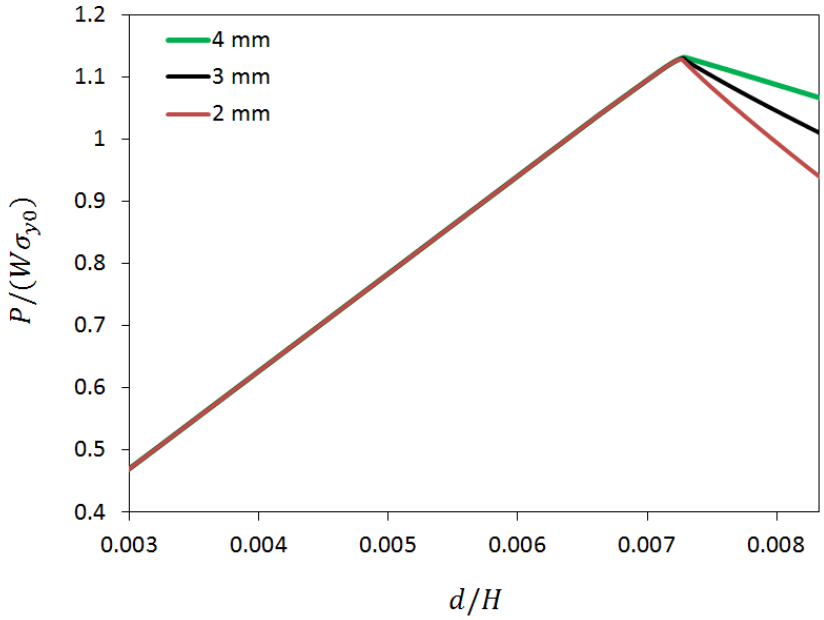

Figure 7: Normalized norm reaction force ($P/(W\sigma_{y0})$) versus normalized displacement (d/H) for different length scales.

curve is illustrated in Fig. 7. The width of the shear band evidently plays a major role on the unloading behavior of the material during the plastic softening stage. Materials with smaller length scale will unload more rapidly, dissipate less energy, and more readily tend toward snap-back behavior and instability. This behavior is similar to that observed in double-edge-notched beams in which materials with smaller fracture toughness experience greater snap-back [47].

The performance of the proposed C^0 methodology for non-local plasticity is also shown by plotting the rate of convergence of the norm of the residual with respect to the number of Newton iterations, illustrated for load step $d/H = 0.0075$ in Fig. 8 for the given displacement steps $\Delta u = 0.002$mm (blue) and $\Delta u = 0.05$mm (red). For small displacement increments on the boundary, the residual converges to zero at a nearly quadratic rate of 1.8. For large displacement increments the convergence rate is much lower, e.g., when displacement load step is $\Delta u = 0.05$mm the rate of convergence of the residual is 0.36.

4.2. Fluid-driven stimulated volume evolution

HF design success depends on a good understanding of the fluid and solid skeleton interactions in relation to the initial in-situ stress field in the subsurface rocks. The large-scale stress condition (far-field stress) is a key parameter controlling the HF propagation path. In this section, we demonstrate the capability of our model to capture SV growth in a naturally fractured rock mass under various far-field in-situ stress conditions. Quantifying the evolution of the SV and the subsequent change in the flow and fluid pressure are the primary interests in this study.

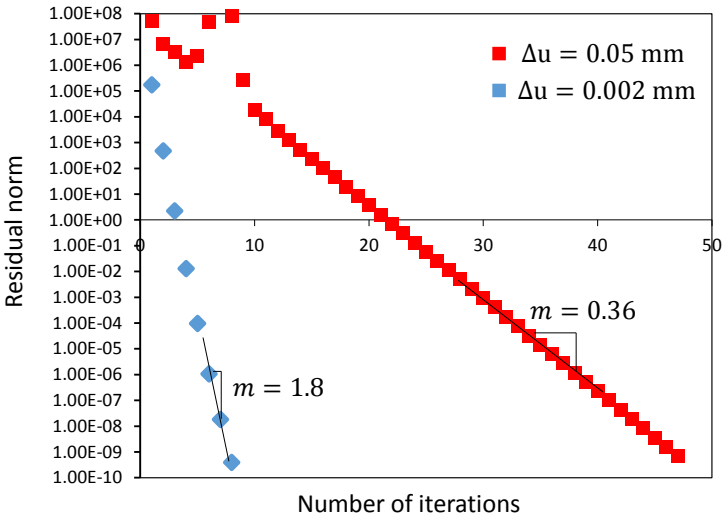

Figure 8: Residual versus the number of iteration at the given displacement $d/H = 0.0075$ for the given displacement steps $\Delta u = 0.002$mm (blue) and $\Delta u = 0.05$mm (red).

Example 1

We consider a synthetic example of injection into a fractured and permeable formation characterized by an internal length scale of 0.45m, initial porosity $\phi = 6\%$, initial permeability $k_0 = 1$md, minimum in-situ stress $\sigma_{min} = -40$MPa acting in the horizontal direction, and maximum in-situ stress $\sigma_{max} = -80$MPa acting in the vertical direction. The liquid is injected at a flow rate of $q = 8 \times 10^{-4}\text{m}^2/\text{s}$ at the center of a 400m^2 square domain (point a), as shown in Fig. 9. Note that at this point we only use arbitrary values of a and b to show the strength of the model. However, these constants in fact can be somewhat constrained by post shut-in flow analysis of a SV. The full discussion of the range of the constant parameters will be discussed in the future. Material parameters used in the simulation are given in Table 2 (chosen based on [48]). The initial virgin permeability of $k_0 = 1$ md is reflective of that of the carbonate rocks.

Figure 10 shows the evolution of the non-local plastic strain and the fluid pressure in time for selected points a, b, and c in the square domain, as marked in Fig. 9. At first, the injection of the fluid causes a rapid increase in the pore pressure at the injection point. The latter, together with the reduction in the effective stress, leads to immediate plastic yielding at the injection point. As more fluid is injected, the plastic yielding then spreads out as the SV grows in a direction generally perpendicular to σ_{min}, as would be expected. Normally, the fluid pressure at the injection point monotonically increases to a peak referred to as the "breakdown" pressure, then it falls, indicating that a tensile fracture is created. The breakdown pressure is a local effect arising from the presence of the borehole. It can be significantly higher than the large-scale fracture closure pressure, which is controlled by the far-field minimum stress. Also, it varies depending on the geomechanical condition of the reservoir, such

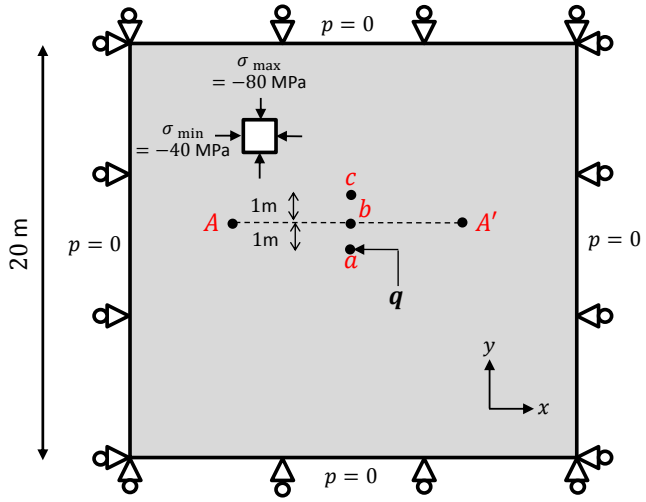

Figure 9: Schematics of the injection problem. A 400m^2 square domain is selected for the injection project. Fluid is injected at at the center of the square domain assuming that its boundary is fixed and drained ($p = 0$). The minimum and maximum confining stresses are $\sigma_{min} = -40$MPa, $\sigma_{max} = -80$MPa, respectively. The line $A - A^{'}$ and points a, b, c will be used later to demonstrate the accuracy of the numerical results.

Injection rate	$q = 0.0008\text{m}^2/\text{s}$
Fluid viscosity	$\mu = 1\text{cP}$
Intermediate in-situ stress	$\sigma_V = -64\text{MPa}$
Shear modulus	$G = 12.0\text{GPa}$
Undrained Poisson's ratio	$\nu_u = 0.30$
Drained Poisson's ratio	$\nu = 0.15$
Initial yield stress	$\sigma_{y0} = 30\text{MPa}$
Characteristic length scale	$l_c = 0.45\text{m}$
Biot's modulus	$M = 29.3\text{GPa}$
Biot's coefficient	$\alpha = 0.64\text{GPa}$
Isotropic softening coefficient	$h = -0.4\text{GPa}$
DP failure constants	$\alpha_f = 0.35$, $\beta = 1$
Initial permeability	$k_0 = 1\text{md}$
Constants in relation (16)	$a = 500000$, $b = 1$

Table 2: Material properties used for the hydraulic fracturing simulations.

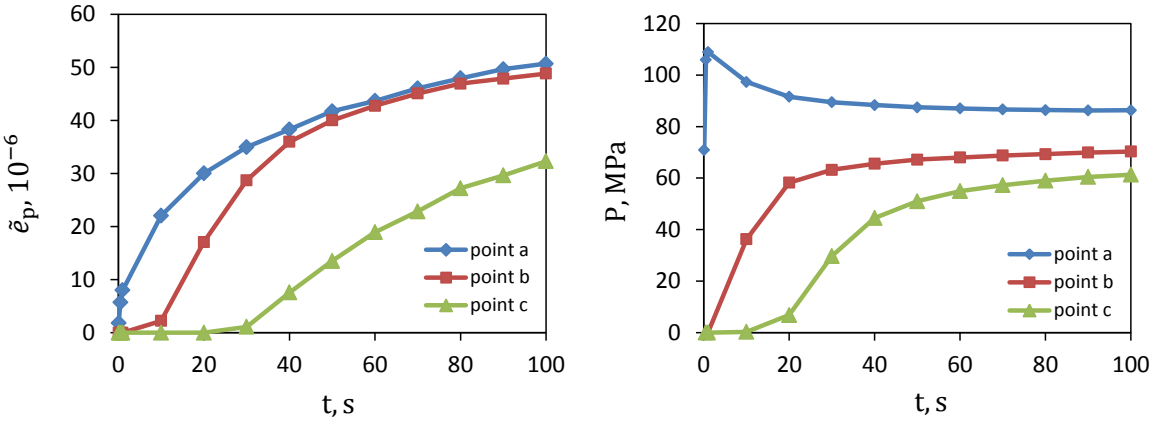

Figure 10: The evolution of the non-local plastic strain and fluid pressure for the given points a, b, and c as marked in Fig. 9. Permeability is related directly to the non-local plastic strain via (16) and as such contour plots of permeability follow the same trend as those of the non-local plastic strain.

as the state of the stress around the injection point, the mechanism of microcracking and failure in the localized plastic zone, and properties of the fluid and the formation. In Fig. 10 a breakdown pressure of about 110MPa can be observed in the injection pressure curve (point a).

Figure 11 shows the contour map of the non-local plastic strain and corresponding pore pressure evolution for three given times, $t = 20$s, $t = 50$s, and $t = 100$s. As expected, given the homogeneity of this synthetic example, the SV volume grows symmetrically from the injection point in the direction of the maximum confining stress, defined by a zone of increased permeability (as permeability is a function of the effective plastic strain). It is an established fact that a HF follows the path of the least resistance, and in the proposed methodology, the SV evolution is not a priori known; it is recovered as the part of the solution, depending on the initial in-situ stress field, and is mesh-independent.

The amount of the SV extension is inversely related to the characteristic length scale of the localized plastic zone. The latter, combined with the far-field stress and other design parameters, determines the amount of work required to propagate the SV. In this study, it is assumed that the characteristic length scale is constant (i.e., that the target formations has homogeneously distributed natural fractures.) In this case, it is reasonable to have a characteristic length scale of the range 0.1m to 1m, as it is expected to be related to the spacing of natural fractures. A similar range of characteristic length scale is previously reported, e.g., in [39]. However, a more realistic representation may require multiple (and possibly spatially variable) length scales introduced as a tensorial quantity to accurately model heterogeneously distributed natural fractures. A characterization of the non-local length scale with site-specific field data, an important factor, is beyond the scope of this paper.

The distribution of the pressure around the fracture also indicates that the fluid diffusion front has propagated far beyond the stimulated region (i.e,. 2-D diffusion).

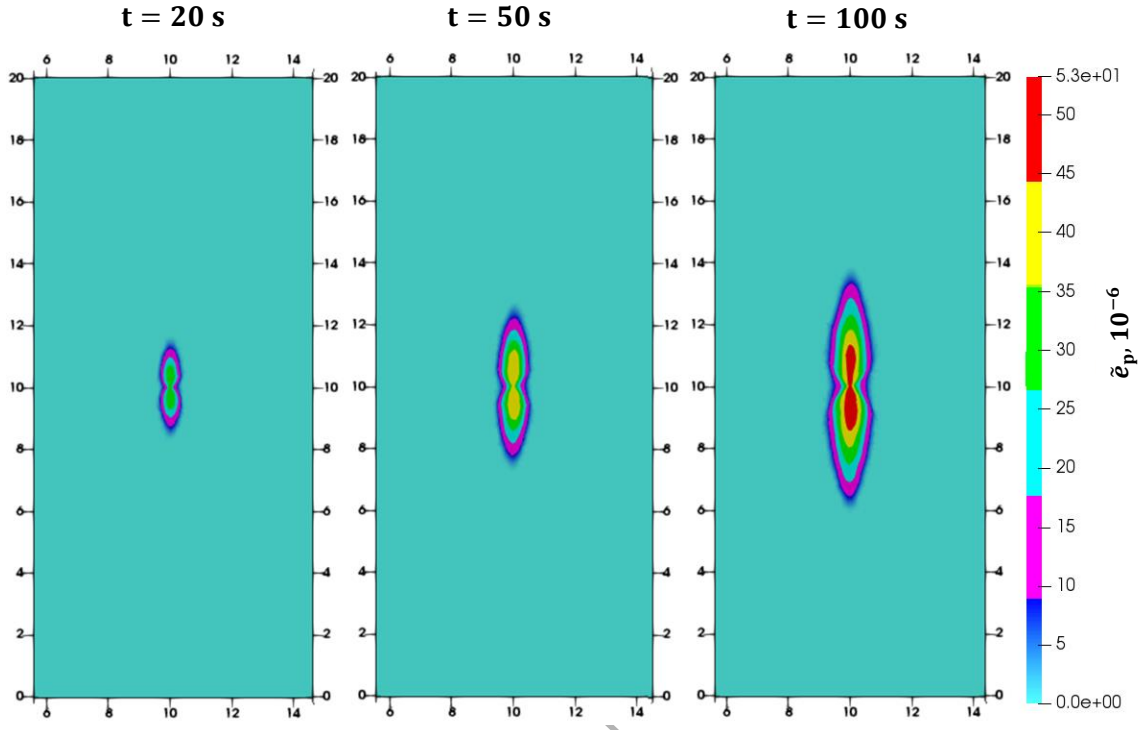

Figure 11: The evolution of the non-local plastic strain for the time steps, $t = 20$ s, $t = 50$ s, and $t = 100$ s. Permeability is related directly to the non-local plastic strain via (16) and as such contour plots of permeability follow the same trend as those of the non-local plastic strain.

This contradicts the conventional HF modeling assumption that the fluid diffusion is limited to a small region around the fracture (1-D diffusion). The latter assumption may only be true for very impermeable reservoirs (shales without open natural fractures), or for the case of high viscosity fluid (gel-like) where filtration processes limit leak-off to the vicinity of the fracture. For the case of low-viscosity injection using water or slickwater (or propane, N_2 or CO_2...), the fluid diffusion can vary over wider ranges of scales from 1-D to 2-D, invalidating the 1-D assumption [5, 49].

Validity of the numerical results

In this section, we investigate the accuracy of the numerical results and the influence of the mesh size on the evolution of the non-local plastic strain and pressure for the proposed methodology. We discretize the domain using three sets of unstructured meshes consisting of 2008 (coarse), 4184 (medium-coarse), and 5665 (fine) elements, shown in Fig. 13. The refinement of mesh size is mainly carried out in the middle region (2m $\times$ 20m) where HF propagation is expected to take place. The minimum element length of the three meshes was $h = 0.06$m, $h = 0.03$m, and $h = 0.01$m.

Figure 14 compares the evolution of the non-local plastic strain and pressure along the cross section line A-A' (Fig. 9) at time $t = 50$s and $t = 100$s for the three meshes. The results for the two finest meshes shows a good agreement for the non-local plastic strain evolution. However, the coarser mesh slightly tends to underpredict and overpredict the non-local plastic strain at $t = 50$s and $t = 100$s,

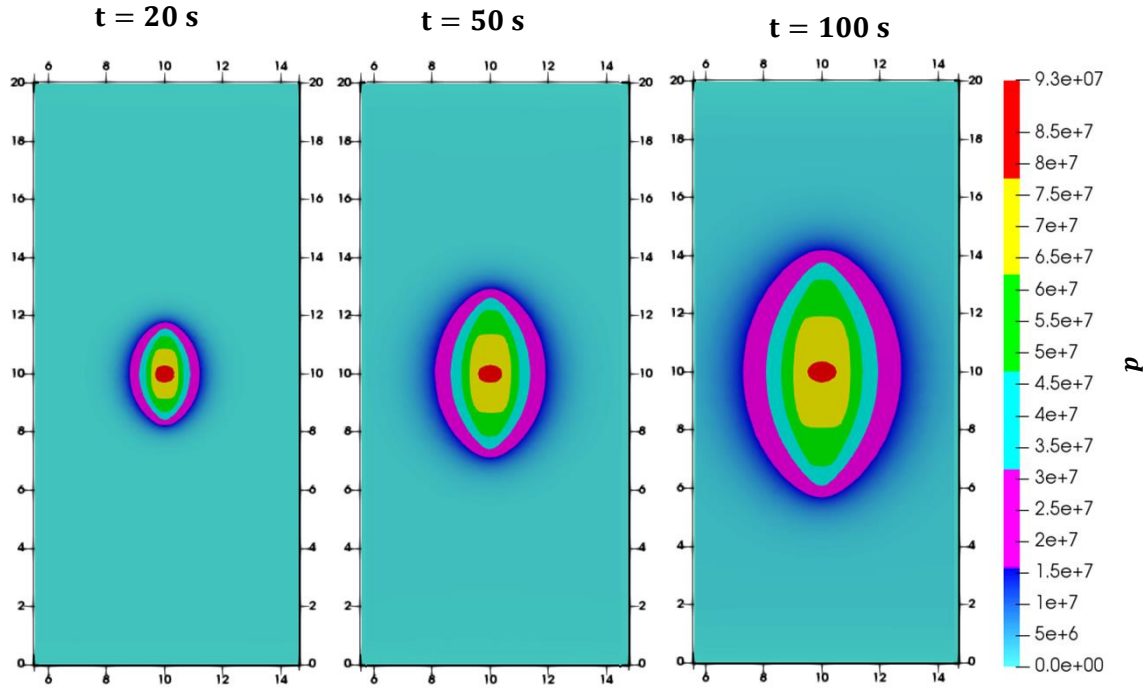

Figure 12: The contours of the fluid pressure for the time steps, $t = 20$s, $t = 50$s, and $t = 100$s.

respectively. The pressure evolution is almost insensitive to the mesh refinement. Since the virgin formation is relatively permeable (1 md), the diffusion front will extend beyond the stimulated volume (plasticity zone). In the stimulated volume, the permeability is higher than that of the surrounding rock mass; as a result, the pressure gradient will be smaller than it would be otherwise.

The convergence of the numerical results in time for non-local plastic strain and injected pressure is also shown for a point 4cm above point a in the Fig. 9. Since the fluid injection takes place at the point in the center of the domain, the fluid pressure becomes singular at the injection point and the numerical results for the pressure at this point converges more slowly. For this reason, we selected a point which is slightly above the injection point. As shown in Fig. 15, the non-local plastic strain results for the two finest meshes are nearly indistinguishable, while the coarse mesh overpredicts the non-local plastic strain. The fluid pressure after early injection times also indicates convergence with mesh refinement.

Example 2-effects of the interface barriers

Although a full discussion of sedimentary layering and geological history effects leading to inhomogeneities in stresses and material properties is beyond our scope, an example is developed here to show the strengths of the proposed method. In this section, we consider an HF example in a formation bounded above and below by formations with greater in-situ confining stresses. In conventional HF simulations, formation properties and the in-situ stress field are commonly assumed to remain unchanged through the entire reservoir. Realistically, the rock mass may contain dis-

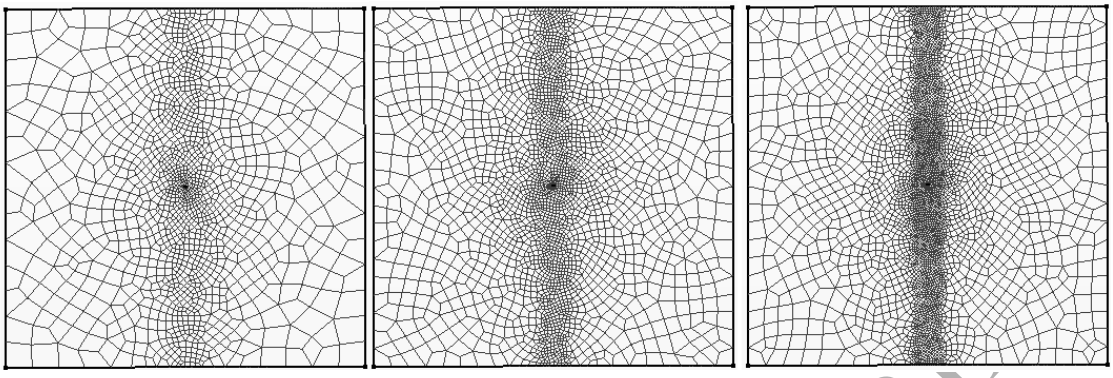

Figure 13: Discretization scheme for the injection problem. Three sets of meshing, coarse (left), medium-coarse (middle), and fine (right) are used for numerical study of the accuracy of the numerical results.

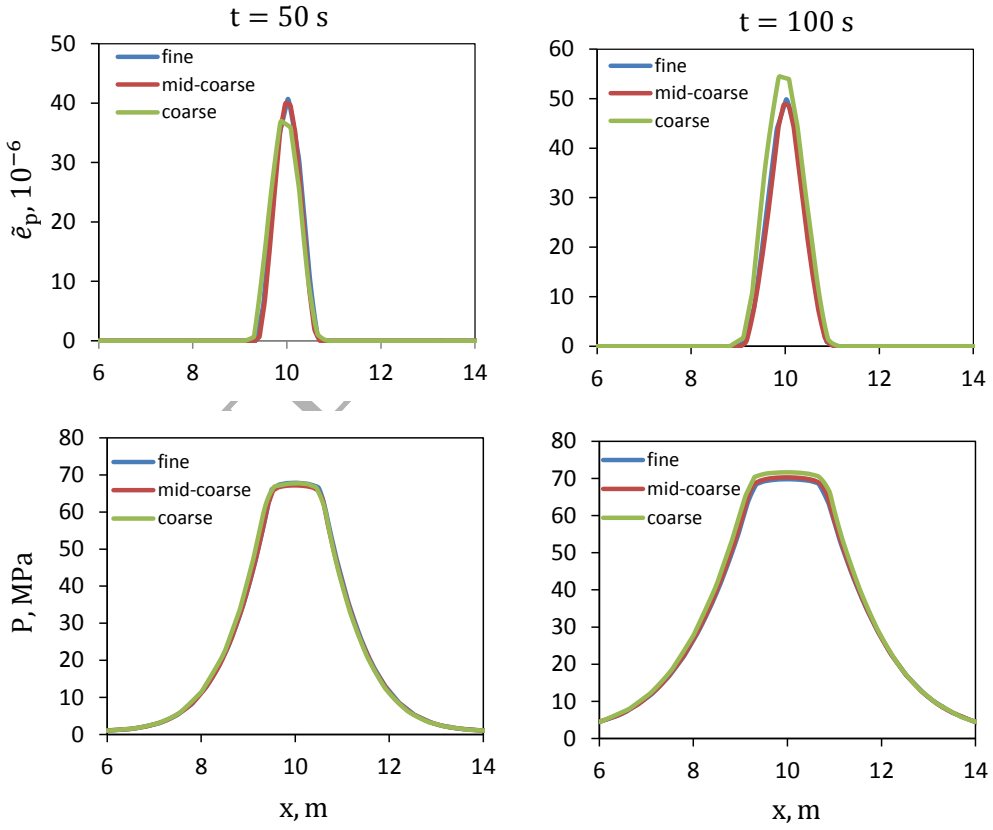

Figure 14: Comparison of the non-local plastic strain and fluid pressure along the line $A - A'$ (marked on the Fig. 9) at the given time $t = 50$s and $t = 100$s. Permeability is related directly to the non-local plastic strain via (16) and as such contour plots of permeability follow the same trend as those of the non-local plastic strain.

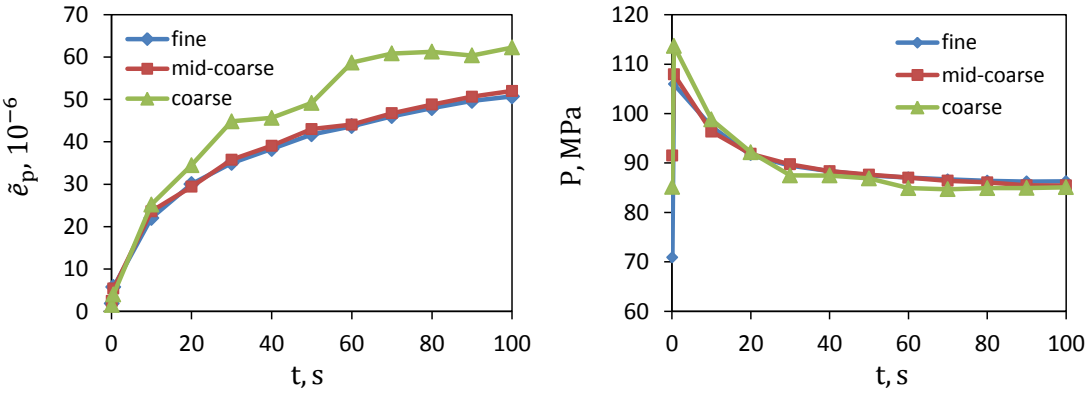

Figure 15: The evolution of the non-local plastic strain and the injected bottom-hole pressure with time for the point a marked on Fig. 9. Permeability is related directly to the non-local plastic strain via (16) and as such contour plots of permeability follow the same trend as those of the non-local plastic strain.

continuities, such as faults, joints, and bedding planes, primarily caused by important geological processes such as tectonics and diagenesis. Formation differences and the frequency and condition of discontinuities often give rise to stress inhomogeneities and significant differences in the bulk (upscaled) mechanical properties of rocks, such as Young's modulus and Poisson's ratio. For example, the stiffer layers characterized by higher Young's modulus and Poisson's ratio tend to accommodate higher tectonic stress, whereas softer rocks are often tectonically relaxed. As the result, HF growth can be significantly restricted or favored by the heterogeneous stress conditions linked to the material properties and the geological history.

The domain described in example 1 is modified by adding two interfaces, each located at a distance of one meter from the injection point, as illustrated in Fig. 16. The interfaces separate the pay-zone from the rest of the domain and are characterized by higher horizontal stresses. The mechanical properties of all three layers are the same and given in Table 2. The other simulation parameters remain unchanged for the sake of simplicity.

Figure 17 shows the evolution of the stimulated zone SV at times $t = 20$s, $t = 50$s, and $t = 100$s. Initially, the SV grows vertically, in the direction perpendicular to the minimum horizontal stress. Following breakdown, the injection pressure continuously decreases as the SV grows vertically, as shown in Fig. 18. The leading edges of the SV reaches the interfaces about $t = 20$s. Whether or not the SV continues to growth vertically or spreads horizontally in the pay-zone depends in a non-trivial way upon both the magnitude of the horizontal in-situ stress in the bounding strata and the vertical in-situ stress in the stimulated formation. In either case, further growth of the SV requires that the net pressure increases, as Fig. 18 shows. In this problem, the elevated horizontal in-situ stresses in the bounding strata are large enough to prevent the SV from continuing to grow vertically. The stimulated zone grows horizontally as the net pressure increases and remains completely contained in the pay-zone. In reality, the combined effect of the formation lithology, the nature of the interface

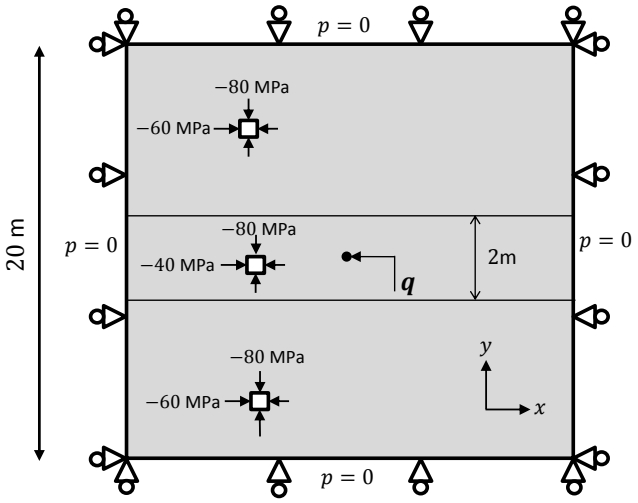

Figure 16: Schematics of the injection problem in the example 2. The minimum and maximum confining stresses for the pay zone the barrier layers are $\sigma_{min} = -40$MPa, $\sigma_{max} = -80$MPa, respectively.

barrier (e.g., horizontal bedding planes), the geological and tectonic history, and the injection parameters all interact to determine the propagation and containment of the SV.

Example 3-effects of stress angle

In this example, the effect of different initial in-situ stress regimes on SV evolution and direction is investigated. We consider four sets of far-field stresses, as illustrated in Fig. 19. The first two sets have non-zero shear components in the vertical and horizontal directions, but the same values of principal stresses as in the previous example. Under some sedimentological and tectonic conditions, for instance, above pinnacle reefs, on the shoulders of salt domes or near a thick channel sand of limited width, the principal stresses may rotate, leading to the possibility of inclined HF propagation [50]. This is shown in Fig. 19a and b where the SV has re-orientated to align with the orientation of the new maximum principal stress which is now inclined at an angle $\beta = \mp 22.5$ with respect to the vertical axis. The HF orientation in an in-situ stress field with no shear components in the vertical and horizontal directions is also correctly captured (Fig. 19c and d).. This example clearly shows the capability of the proposed methodology to determine the expected path, independently of the mesh topology.

5. Conclusions

Microseismic monitoring of hydraulic fracturing in naturally fractured rocks confirms the existence of a stimulated region of Mode I and Mode II or III fracturing deformations, evidenced as a roughly ellipsoidal cloud of stick-slip (Mode II, III) events. To simulate this behavior, a novel mathematical approach that can emulate the evolution of the stimulated volume during hydraulic fracturing of naturally

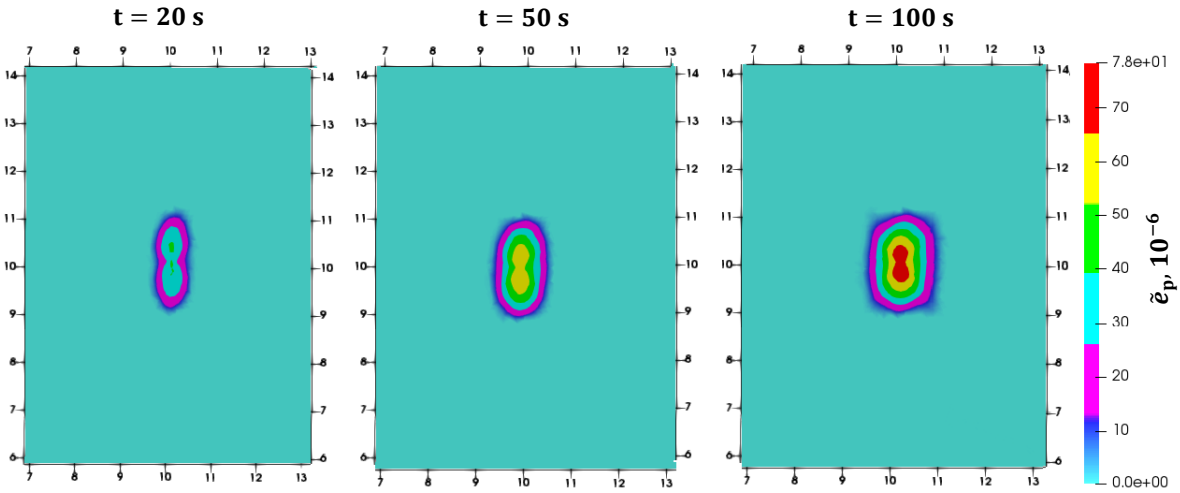

Figure 17: The evolution of the non-local plastic strain for the time steps, $t = 20$s, $t = 50$s, and $t = 100$s. Permeability is related directly to the non-local plastic strain via (16) and as such contour plots of permeability follow the same trend as those of the non-local plastic strain.

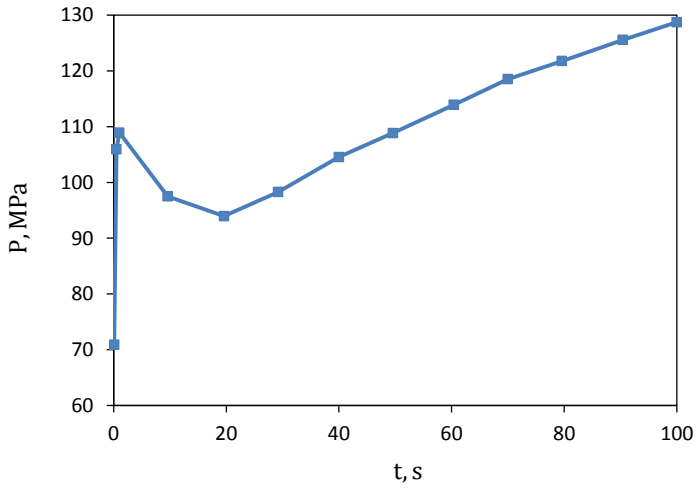

Figure 18: The evolution of the injected bottom hole pressure with time for the example 2.

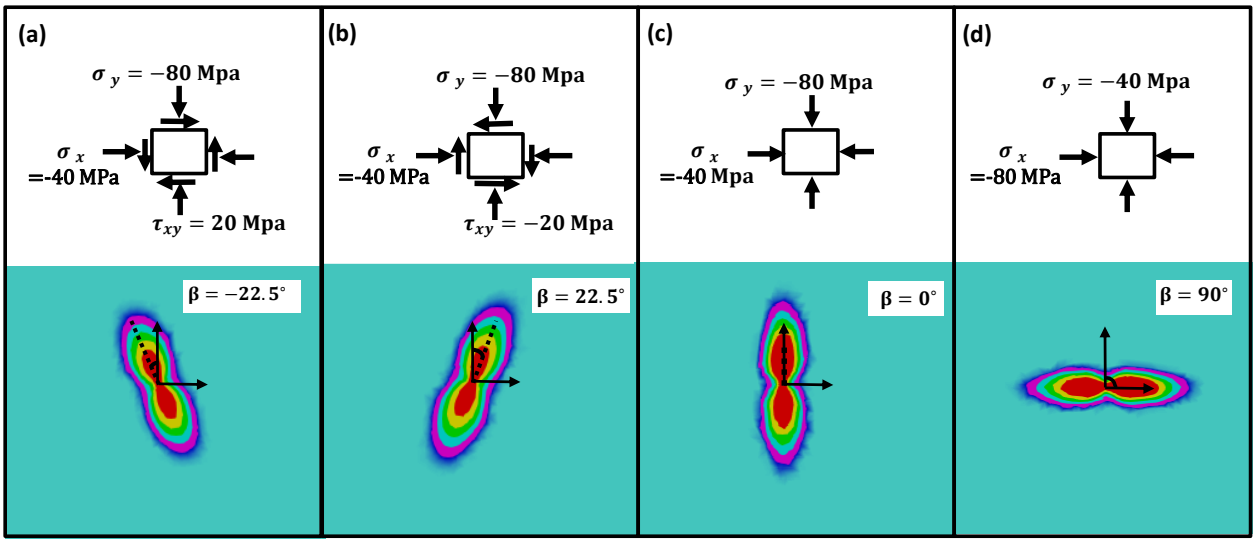

Figure 19: The effects of the stress angle on the stimulated volume orientation. Permeability is related directly to the non-local plastic strain via (16) and as such contour plots of permeability follow the same trend as those of the non-local plastic strain.

fractured rocks is developed. This is achieved by defining an equivalent non-local poro-elastic-plastic continuum zone for the stimulated region, described by an internal characteristic length scale. The elastic-plastic constitutive model is combined with Biot's poroelastic theory to account for the interaction of the fluid and solid deformations. We propose a new implicit C^0 continuous Finite Element Analysis, which in the stress and plastic strain updates are realized using a modified corrector-predictor return algorithm. To improve the performance of the Newton-Raphson solver, a consistent algorithmic tangent operator for the non-local plastic flow rule is also developed. For verification, a mesh-independent study of the proposed non-local plasticity model for the standard non-porous biaxial compression test was performed. The effectiveness of the coupled poro-elastic-plastic model was then tested for several hydraulic fracturing example problems. The stimulated zone and the fluid pressure in relation to the local in-situ stress field were accurately quantified. We also showed that the proposed methodology is capable of determining the path of a priori unknown hydraulic fracturing enhanced zone propagation. This model provides a new tool to better quantify the stimulated zone, which can lead to better fracture design and subsequent well performance.

Acknowledgments

The authors gratefully acknowledge the support of a Discovery Grant and a Strategic Grant from the Natural Sciences and Engineering Research Council of Canada (NSERC) for the early stages of the research and a NSERC Discovery Grant for the later stages.

References

References

[1] M. J. Economides and K. G. Nolte, editors. *Reservoir Stimulation*. John Wiley & Sons, Chichester UK, 3rd edition, 2000.

[2] R. G. Jeffrey and K. W. Mills. Hydraulic fracturing applied to inducing longwall coal mine goaf falls. In J. Girard, M. Liebman, C. Breeds, and T. Doe, editors, *Pacific Rocks 2000 – Proc. 4th North American Rock Mechanics Symp.*, pages 423–430, Rotterdam, 2000. Balkema.

[3] A. van As and R. G. Jeffrey. Caving induced by hydraulic fracturing at Northparkes mines. In *Pacific Rocks 2000*, pages 353–360, Rotterdam, 2000. Balkema.

[4] D.I. Harris, R.J. Mair, J.P. Love, R.N. Taylor, and T.O. Henderson. Observations of ground and structure movements for compensation grouting during tunnel construction at waterloo station. *Geotechnique*, 1994.

[5] E. Sarvaramini and D.I. Garagash. Breakdown of a pressurized fingerlike crack in a permeable solid. *Journal of Applied Mechanics*, 82(6):061006, 2015.

[6] Z.A. Moschovidis, D.C. Gardner, and R.W. Veatch. Disposal of oily cuttings by downhole periodic fracturing injections, Valhall, North Sea: case study and modeling concepts: SPEDC 9 (4): 256–262. *Trans., AIME*, 297:256–262, December 1994.

[7] S. Maxwell. *Microseismic imaging of hydraulic fracturing: Improved engineering of unconventional shale reservoirs*. Society of Exploration Geophysicists, 2014.

[8] M.B. Dusseault, J. McLennan, and J. Shu. Massive multi-stage hydraulic fracturing for oil and gas recovery from low mobility reservoirs in China. *Petroleum Drilling Techniques*, 39(3):6–16, 2011.

[9] M.B. Dusseault. Geomechanical aspects of shale gas development. *Rock Mechanics for Resources, Energy and Environment*, 39, 2013.

[10] X. Weng, O. Kresse, C.E. Cohen, R. Wu, and H. Gu. Modeling of hydraulic fracture network propagation in a naturally fractured formation. In *SPE Hydraulic Fracturing Technology Conference*. Society of Petroleum Engineers, 2011.

[11] M.J. Mayerhofer, E. Lolon, N.R. Warpinski, C. L. Cipolla, D. W. Walser, and C. M. Rightmire. What is stimulated reservoir volume? *SPE Production & Operations*, 25(01):89–98, 2010.

[12] C.L. Cipolla, N.R. Warpinski, M. Mayerhofer, E.P. Lolon, and M. Vincent. The relationship between fracture complexity, reservoir properties, and fracture-treatment design. *SPE production & Operations*, 25(04), 2010.

[13] E. Detournay, J. I. Adachi, and D. I. Garagash. Asymptotic and intermediate asymptotic behavior near the tip of a fluid-driven fracture propagating in a permeable elastic medium. In A. V. Dyskin, X. Hu, and E. Sahouryeh, editors, *Structural Integrity and Fracture*, pages 9–18, Lisse, 2002. Balkema.

[14] A. P. Bunger, E. Detournay, D. I. Garagash, and A. P. Peirce. Numerical simulation of hydraulic fracturing in the viscosity-dominated regime (spe 106115). In *SPE Hydraulic Fracturing Technology Conference*, pages 1–11, College Station, Texas, January 2007.

[15] A. P. Bunger, E. Detournay, and D. I. Garagash. Toughness-dominated hydraulic fracture with leak-off. *Int. J. Fracture*, 134:175–190, 2005.

[16] P. Fu, S.M. Johnson, and C.R. Carrigan. An explicitly coupled hydro-geomechanical model for simulating hydraulic fracturing in arbitrary discrete fracture networks. *International Journal for Numerical and Analytical Methods in Geomechanics*, 37(14):2278–2300, 2013.

[17] M.C. Cacas, E. Ledoux, G.D. Marsily, B. Tillie, A. Barbreau, E. Durand, B. Feuga, and P. Peaudecerf. Modeling fracture flow with a stochastic discrete fracture network: calibration and validation: 1. the flow model. *Water Resources Research*, 26(3):479–489, 1990.

[18] B. Loret and J.H. Prevost. Dynamic strain localization in fluid-saturated porous media. *Journal of Engineering Mechanics*, 117(4):907–922, 1991.

[19] B.A. Schrefler, C. E. Majorana, and L. Sanavia. Shear band localization in saturated porous media. *Archives of Mechanics*, 47(3):577–599, 1995.

[20] H. Shimizu, S. Murata, and T Ishidab. The distinct element analysis for hydraulic fracturing in hard rock considering fluid viscosity and particle size distribution. *International Journal of Rock Mechanics and Mining Sciences*, 48(5):712–727, 2011.

[21] B. Damjanac, I. Gil, M. Pierce, M. Sanchez, A. Van As, and J. McLennan. A new approach to hydraulic fracturing modeling in naturally fractured reservoirs. In *44th US Rock Mechanics Symposium and 5th US-Canada Rock Mechanics Symposium*, 2010.

[22] M. Yetisir, R. Gracie, and M. Dusseault. Up-scaling DEM simulations. American Rock Mechanics Association, 2016.

[23] M. Jirasek. Nonlocal models for damage and fracture: comparison of approaches. *International Journal of Solids and Structures*, 35(31-32):4133–4145, 1998.

[24] Z.P. Bazant and M. Jirasek. Nonlocal integral formulations of plasticity and damage: survey of progress. *Journal of Engineering Mechanics*, 128(11):1119–1149, 2002.

[25] J.W. Rudnicki and J.R. Rice. Conditions for the localization of deformation in pressure-sensitive dilatant materials. *Journal of the Mechanics and Physics of Solids*, 23(6):371–394, 1975.

[26] Z.P. Bazant and B. H. Oh. Crack band theory for fracture of concrete. *Materiaux et Construction*, 16(3):155–177, 1983.

[27] R. De Borst and J. Pamin. Some novel developments in finite element procedures for gradient-dependent plasticity. *International Journal for Numerical Methods in Engineering*, 39(14):2477–2505, 1996.

[28] J. Pamin. *Gradient-Dependent Plasticity in Numerical Simulation of Localization Phenomena*. PhD thesis, 1994.

[29] S. Busetti, K. Mish, P.Hennings, and Z. Reches. Damage and plastic deformation of reservoir rocks: Part 2. propagation of a hydraulic fracture. *AAPG bulletin*, 96(9):1711–1732, 2012.

[30] S. Busetti, K. Mish, and Z. Reches. Damage and plastic deformation of reservoir rocks: Part 1. damage fracturing. *AAPG bulletin*, 96(9), 2012.

[31] M. Nassir, A. Settari, and R.G. Wan. Prediction of stimulated reservoir volume and optimization of fracturing in tight gas and shale with a fully elasto-plastic coupled geomechanical model. *SPE Journal*, 19(05):771–785, 2014.

[32] D.C. Drucker and W. Prager. Soil mechanics and plastic analysis or limit design. *Quarterly of Applied Mathematics*, 10(2):157–165, 1952.

[33] J. Pamin and R. De Borst. A gradient plasticity approach to finite element predictions of soil instability. *Archives of Mechancis*, 47:353–377, 1995.

[34] R.A.B. Engelen. *Plasticity-induced damage in metals : nonlocal modelling at finite strains*. PhD thesis, 2005.

[35] R.A.B. Engelen, M.G.D. Geers, and F.P.T. Baaijens. Nonlocal implicit gradient-enhanced elasto-plasticity for the modelling of softening behaviour. *International Journal of Plasticity*, 19(4):403–433, 2003.

[36] J.C. Simo and R.L.Taylor. Consistent tangent operators for rate-independent elastoplasticity. *Computer Methods in Applied Mechanics and Engineering*, 48(1):101–118, 1985.

[37] C. Miehe, S. Mauthe, and S. Teichtmeister. Minimization principles for the coupled problem of darcy–biot-type fluid transport in porous media linked to phase field modeling of fracture. *Journal of the Mechanics and Physics of Solids*, 82:186–217, 2015.

[38] A. Mikelic, M.F. Wheeler, and T. Wick. Phase-field modeling of a fluid-driven fracture in a poroelastic medium. *Computational Geosciences*, 19(6):1171–1195, 2015.

[39] M. E. Mobasher, L. Berger-Vergiat, and H. Waisman. Non-local formulation for transport and damage in porous media. *Computer Methods in Applied Mechanics and Engineering*, 324:654–688, 2017.

[40] M.F. Wheeler, T. Wick, and W. Wollner. An augmented-lagrangian method for the phase-field approach for pressurized fractures. *Computer Methods in Applied Mechanics and Engineering*, 271:69–85, 2014.

[41] A.H. Delgoshaie, D.W. Meyer, P. Jenny, and H.A. Tchelepi. Non-local formulation for multiscale flow in porous media. *Journal of Hydrology*, 531:649–654, 2015.

[42] M. Sen and E. Ramos. A spatially non-local model for flow in porous media. *Transport in Porous Media*, 92:29–39, 2012.

[43] W. Prager. Theory of plasticity: a survey of recent achievements. *Proc. Instn. Mech. Engrs*, 169:41–57, 1955.

[44] Ivo Babuška. Error-bounds for finite element method. *Numerische Mathematik*, 16(4):322–333, 1971.

[45] J.C. Simo and T.J.R. Hughes. *Computational Inelasticity*, volume 7. Springer Science & Business Media, 2006.

[46] J.K. Djoko, F. Ebobisse, A.T. McBride, and B.D. Reddy. A discontinuous Galerkin formulation for classical and gradient plasticity. part 2: Algorithms and numerical analysis. *Computer Methods in Applied Mechanics and Engineering*, 197(1):1–21, 2007.

[47] A. Zamani, R. Gracie, and M.R. Eslami. Cohesive and non-cohesive fracture by higher-order enrichment of XFEM. *International Journal for Numerical Methods in Engineering*, 90(4):452–483, 2012.

[48] E. Detournay and A. H.-D. Cheng. Analysis and design methods: Comprehensive rock engineering: Principles, practice and projects. 2:113, 2014.

[49] E. Sarvaramini and D.I. Garagash. Poroelastic effects in reactivation of a finger-like hydraulic fracture. *Journal of Applied Mechanics*, 83(6):061011, 2016.

[50] M.B. Dusseault, V. Maury, F. Sanfilippo, and F.J. Santarelli. Drilling through salt: constitutive behavior and drilling strategies. In *Gulf Rocks 2004, the 6th North America Rock Mechanics Symposium (NARMS)*. American Rock Mechanics Association, 2004.